Intra-condensate demixing of TDP-43 inside stress granules generates pathological aggregates

Xiao Yan[1], David Kuster[1,9], Priyesh Mohanty[3,9], Jik Nijssen[1,9], Karina Pombo-García[1,9], Azamat Rizuan[3], Titus M. Franzmann[2], Aleksandra Sergeeva[1,2], Patricia M. Passos[4], Leah George[4], Szu-Huan Wang[5], Jayakrishna Shenoy[5], Helen L. Danielson[6], Alf Honigmann[2], Yuna M. Ayala[4], Nicolas L. Fawzi[5], Jeetain Mittal[3,7,8,*], Simon Alberti[2,*], Anthony A. Hyman[1,10,*]

AFFILIATIONS

[1]Max Planck Institute of Molecular Cell Biology and Genetics (MPI-CBG); Dresden, Saxony, 01307; Germany

[2]Biotechnology Center (BIOTEC), Center for Molecular and Cellular Bioengineering, Technische Universität Dresden; Dresden, Saxony, 01307; Germany

[3]Artie McFerrin Department of Chemical Engineering, Texas A&M University; College Station, TX 77843; USA

[4]Edward Doisy Department of Biochemistry and Molecular Biology, Saint Louis University; St. Louis, MO 63104; USA

[5]Department of Molecular Biology, Cell Biology & Biochemistry, Brown University; Providence, RI 02912; USA

[6]Center for Biomedical Engineering, Brown University; Providence, RI 02912; USA

[7]Department of Chemistry, Texas A&M University; College Station, TX 77843; USA

[8]Interdisciplinary Graduate Program in Genetics and Genomics, Texas A&M University; College Station, TX 77843; USA

[9]These authors contributed equally

[10]Lead contact

*Correspondence: hyman@mpi-cbg.de (A.A.H.), simon.alberti@tu-dresden.de (S.A.), jeetain@tamu.edu (J.M.)

SUMMARY

Cytosolic aggregation of the nuclear protein TDP-43 is associated with many neurodegenerative diseases, but the triggers for TDP-43 aggregation are still debated. Here, we demonstrate that TDP-43 aggregation requires a double event. One is up-concentration in stress granules beyond a threshold, and the other is oxidative stress. These two events collectively induce intra-condensate demixing, giving rise to a dynamic TDP-43 enriched phase within stress granules, which subsequently transitions into pathological aggregates. Mechanistically, intra-condensate demixing is triggered by local unfolding of the RRM1 domain for intermolecular disulfide bond formation and by increased hydrophobic patch interactions in the C-terminal domain. By engineering TDP-43 variants resistant to intra-condensate demixing, we successfully eliminate pathological TDP-43 aggregates in cells. We conclude that up-concentration inside condensates and simultaneous exposure to environmental stress could be a general pathway for protein aggregation, with intra-condensate demixing constituting a key intermediate step.

KEYWORDS

TDP-43, neurodegenerative diseases, ALS, protein aggregation, phase separation, stress granules, intra-condensate demixing, multiphasic condensate

INTRODUCTION

A key hallmark of most neurodegenerative diseases is the formation of protein aggregates. For instance, aggregates of Tau protein are associated with Alzheimer's disease, and aggregates of α-synuclein are associated with Parkinson's disease. Test tube experiments with purified disease-causing proteins have shown that proteins in isolation are soluble in solution.[1,2] Their aggregation typically is a rare, concentration-dependent event that requires a structural destabilization induced by changes in physical-chemical conditions or genetic mutations. In cells the very same proteins are typically highly soluble, despite the crowded intracellular milieu.[3] For example, overexpression of Tau or α-synuclein is insufficient to generate protein aggregates in cells.[4–7]

The stability of disease-causing proteins poses the following question: Where and how do pathological protein aggregates arise in the intracellular environment? In particular, what are the actual triggers for a soluble protein to become insoluble and initiate the aggregation process?

One of the most devastating neurodegenerative diseases is amyotrophic lateral sclerosis (ALS), a motor neuron disease that commonly results in loss of motor neurons and death within a few years of onset of symptoms. The protein most frequently associated with ALS is the nuclear TAR DNA-binding protein 43 (TDP-43). TDP-43 has essential functions in transcriptional regulation, pre-mRNA splicing and translation regulation.[8–11] TDP-43 predominantly localizes to the nucleus because of a nuclear localization signal that is recognized by importins.[12,13] The cytosolic TDP-43 concentration is low under physiological conditions, but under stress it passively leaks into the cytoplasm.[14] Mis-localized cytosolic TDP-43 forms aggregates in ~97% of ALS, ~45% of frontotemporal dementia (FTD), and all cases of Alzheimer's disease-associated LATE (Limbic-predominant Age-related TDP-43 Encephalopathy), suggesting that nuclear depletion and cytoplasmic aggregation of TDP-43 is a general hallmark of several age-related neurodegenerative diseases.[15–19] The cytoplasmic accumulation and aggregation of TDP-43 could confer a loss-of-function by mis-localizing, and/or a gain-of-toxicity by sequestration of essential cellular factors.[13,20–24] Therefore,

a central challenge in ALS research is to identify the triggers for wild-type TDP-43 aggregation.

The aggregation of TDP-43 is thought to be driven by a structural change of an α-helical region in the C-terminus that transitions into a cross-β sheet structure.[25,26] This structural transition has been shown to be accelerated by disease mutations in the α-helical region,[27] although TDP-43 aggregation also occurs in the absence of mutations in most ALS cases. However, although the structural transitions that lead to aggregated TDP-43 are well studied, the actual triggers that induce the onset of aggregation in the cellular context remain unknown. Oxidative stress has been implicated as an environmental trigger,[28] but the relationship between oxidative stress and structural destabilization of TDP-43 remains to be determined. This lack of understanding hinders the development of therapeutic agents.

Human genetics suggests a strong connection between ALS and a type of biomolecular condensate called a stress granule.[29–33] Stress granules are canonical condensates in the eukaryotic cytosol that are triggered by various stresses and assemble *via* interactions between RNA and RNA-binding proteins.[34–36] Because many of these stress granule-associated RNA-binding proteins have been linked to ALS, it has been hypothesized that stress granules could in part be crucibles of such diseases.[31] However, the role of cellular condensates in promoting aggregation of TDP-43 is controversial. Patient data have shown that pathological TDP-43 aggregates contain key stress granule proteins such as TIA-1, eIF3, and PABP-1.[37–39] Indeed, a recent histopathological examination, using patient samples, indicated the presence of the stress granule marker HuR in early-stage ALS spinal cord inclusions.[40] However, other work has suggested that aggregation occurs outside rather than inside stress granules and has proposed that stress granules might protect against aggregation.[24,41–46] These disparate results have made it difficult to come to any general conclusions about the role of stress granule condensates in TDP-43 aggregation.

Here, we investigate the role of stress granules in TDP-43 aggregation. Using biochemical reconstitution, biophysical analysis, computational simulations and genetic experiments in cells, we show that aggregation of TDP-43 requires a double event. One event is that stress granules raise the concentration of

cytosolic TDP-43 above a critical threshold. The other event is oxidative stress, which leads to cysteine oxidation. Together, these two events induce an intra-condensate demixing process, giving rise to a TDP-43 enriched phase within stress granules. The demixing process is driven by local unfolding of the RRM1 domain for cysteine oxidation and disulfide bond formation, and by increased hydrophobic patch interactions in the C-terminal domain. These condensates then harden to form aggregates with pathological hallmarks, in both HeLa cells but also neurons derived from iPS cells. By engineering TDP-43 variants that are resistant to intra-condensate demixing, we successfully eliminate pathological TDP-43 aggregates in cells. Together, our findings reveal that stress granules can act as crucibles triggering TDP-43 aggregation *via* a key intra-condensate demixing process. We suggest the combination of increased concentration within condensates and simultaneous exposure to environmental stress could be a general mechanism for *de novo* protein aggregation in cells.

RESULTS

TDP-43 undergoes intra-condensate demixing inside stress granules

TDP-43 is primarily a nuclear protein under physiological conditions, where it regulates the splicing of multiple genes. Cytoplasmic aggregation requires it to leave the nucleus. To decouple the process of nucleocytoplasmic shuttling from aggregation in the cytoplasm, we transfected HeLa cells with a GFP-tagged TDP-43 variant in which the nuclear localization signal (NLS) was disrupted (TDP-43$^{\Delta NLS}$).[47] After stressing cells by adding 100 μM arsenite, we noticed three different cellular phenotypes. Two of those have previously been observed: 1) cells with dispersed TDP-43$^{\Delta NLS}$ in stress granules,[37] 2) cells exhibiting large TDP-43$^{\Delta NLS}$ aggregates independent of stress granules.[24,46] However, we also noticed that in many cells TDP-43$^{\Delta NLS}$ showed a punctate distribution inside stress granules.

Plasmid transfection resulted in populations of cells with a ten-fold variation in cytosolic TDP-43$^{\Delta NLS}$ concentration. To investigate whether the observed phenotypes are related to protein concentration, we determined cytosolic TDP-43$^{\Delta NLS}$ expression levels before stress (**Figures 1A** and **S1A**). Cells exhibiting the above three distinct behaviors correlated strongly with low (~0.2–0.4 μM), high (~0.8–4.0 μM) and medium (~0.4–0.7 μM) expression of

TDP-43$^{\Delta NLS}$ (**Figure 1A**). It is noteworthy that the endogenous concentration of TDP-43 in HeLa cells is approximately 0.5 μM,[48] which falls within the medium expression range but not in high expression cells.

In low expression cells, TDP-43$^{\Delta NLS}$ was diffuse in the cytoplasm before stress (**Figure S1B**), and after stress accumulated in stress granules where it remained dispersed and dynamic, as assayed by fluorescence recovery after photobleaching (FRAP) (**Figures 1A**, **S1C**, and **Video S1**). In high expression cells, TDP-43$^{\Delta NLS}$ assembled into condensates before stress, which were dynamic, with an average diameter of ~1.1 μm (**Figures S1B** and **S1D**). Upon adding 100 μM arsenite to stress the cells, these TDP-43$^{\Delta NLS}$ condensates rapidly transformed into aggregates (**Figure S1D**), and remained independent of stress granules (**Figure 1A** and **Video S2**). This transition of dynamic condensates to less dynamic aggregates is in agreement with previous studies.[24,46]

In medium expression cells, TDP-43$^{\Delta NLS}$ was diffuse before stress (**Figure S1B**). However, after stress, TDP-43$^{\Delta NLS}$ was locally concentrated and formed puncta inside stress granules (**Figure 1A**). The time evolution of a representative stress granule exhibiting TDP-43$^{\Delta NLS}$ puncta is shown in **Figure 1B** and **Video S3**. Initially, TDP-43$^{\Delta NLS}$ was uniformly dispersed inside stress granules, but after 30 min of stress, distinct TDP-43 puncta emerged that excluded the stress granule marker G3BP1 (**Figure 1B**). We name this phenomenon of TDP-43$^{\Delta NLS}$ puncta formation inside stress granules *intra-condensate demixing*, as it is accompanied by the formation of two distinct condensed phases.

Stimulated emission depletion microscopy imaging (STED; see STAR Methods) confirmed that intra-condensate demixing occurs (**Figure 1C**). With longer exposure to stress (120 min), TDP-43$^{\Delta NLS}$ showed marked separation from G3BP1. This was accompanied by a change in TDP-43$^{\Delta NLS}$ morphology from the distributed spherical condensates to irregularly shaped structures, eventually giving rise to fragmented stress granules (**Figure 1C**). We also confirmed that intra-condensate demixing occurs for wild-type TDP-43 containing a functional NLS (**Figure S1E**).

Intra-condensate demixing of TDP-43 results in pathological aggregation

Demixed TDP-43 puncta exhibited a liquid-like behavior, as indicated by droplet fusion (**Figure S1F**). However, the dynamics of TDP-43 protein gradually slowed over time, as studied by FRAP analysis (**Figure 1D**). The internal concentration of individual TDP-43 puncta was further elevated compared to their state before demixing inside stress granules (**Figure S1G**), a process that has been coupled to a liquid-to-solid transition.[49]

We tested whether the demixed TDP-43 shows aggregation hallmarks using three commonly used markers: recruitment of heat shock proteins, ubiquitination and phosphorylation. Ubiquitination and phosphorylation are two commonly found pathological hallmarks of TDP-43 inclusions in ALS and FTD patients.[15,50,51] HSPB1, a small heat shock protein which was shown previously to interact with misfolded TDP-43,[46] weakly localized to stress granules before intra-condensate demixing (**Figure 1E**). However, upon prolonged stress, HSPB1 strongly co-stained with demixed TDP-43$^{\Delta NLS}$ puncta (**Figure 1E**). TDP-43$^{\Delta NLS}$ puncta also exhibited strong ubiquitin signal and were recognized with an antibody specific for phosphorylation at Ser409/410 (**Figures 1F** and **S1H**).

By visualizing poly(A)-containing mRNA using an Atto647N-labeled oligo-dT oligonucleotide, we observed that the colocalization between demixed TDP-43$^{\Delta NLS}$ and mRNA was lost upon prolonged stress (**Figure 1G**). This suggests that TDP-43 is losing its structure or function as an RNA-binding protein.[11,52] Demixed TDP-43$^{\Delta NLS}$ puncta recruited nuclear TDP-43 into these cytoplasmic aggregates (**Figure S1I**), suggesting that aggregates generated *via* intra-condensate demixing could cause a gain-of-toxicity effect by sequestering key cellular factors.[33,53,54]

Taken together, our data so far show that if the TDP-43 concentration exceeds a threshold concentration after partitioning into stress granules, it will undergo intra-condensate demixing and assemble into a TDP-43 enriched phase. Inside this phase, TDP-43 dynamics slow down and the protein starts to form pathological aggregates.

Intra-condensate demixing of TDP-43 promotes a liquid-to-solid phase transition in reconstituted stress granules

220 We used *in vitro* reconstitution to demonstrate that intra-condensate demixing is a distinct phase separation-driven process within multicomponent stress granules. For this purpose, we employed a minimal stress granule system that is based on purified G3BP1 and RNA[34] (**Figure 2A;** see STAR Methods). TDP-43 readily partitioned into these minimal stress granules and colocalized 225 well with G3BP1 (**Figure 2A**). Strikingly, initially well-mixed TDP-43 formed a separate phase inside stress granules over time, which excluded G3BP1 (**Figure 2B** and **Video S4**), similar to the intra-condensate demixing observed in cells (**Figure 1B**). By calculating the Pearson correlation between the fluorescence intensities of TDP-43 and G3BP1 and setting an apparent 230 demixing threshold of 0.85, TDP-43 demixing occurred after 5–6 h (**Figure 2B**). Quantifying TDP-43 concentration before demixing (0–4 h) revealed that stress granules continuously concentrated TDP-43 to cross a threshold for intra-condensate demixing (**Figure 2C**).

Deleting the RNA-recognition motifs RRM1 and RRM2 (ΔRRM1-2) strongly 235 reduced TDP-43 partitioning into stress granules (**Figure 2A**), suggesting that TDP-43 recruitment depends on its RNA binding. However, when demixed, the TDP-43-rich phase contained less RNA than the G3BP1-rich phase (**Figure S2A**), consistent with loss of RNA binding in cells (**Figure 1G**). Demixed TDP-43 puncta fused (**Figure 2D**), suggesting their liquid-like property. 240 TDP-43 puncta tended to orient towards the periphery of stress granules (**Figure 2E**). Thus, our *in vitro* system showed that reconstituted minimal stress granules can drive the formation of a TDP-43 enriched phase, giving rise to multiphasic condensates.

After intra-condensate demixing, TDP-43 concentration remained constant in 245 the mixed phase, while it progressively increased in the demixed phase (5–10 h, **Figure 2C**), indicating that demixed TDP-43 phase may undergo a liquid-to-solid transition.[49] Evidence that the demixed TDP-43 phase leads to TDP-43 misfolding and aggregation came from the following experiments: First, mixed TDP-43 inside stress granules was dynamic by FRAP analysis, while 250 demixed TDP-43 displayed aging over time and protein dynamics gradually slowed down (**Figures 2F** and **S2B**). Second, the aging of demixed TDP-43 also coincided with increased staining with an aggregation-specific amytracker

dye and detection of oligomers by semi-denaturing agarose gel electrophoresis (SDD-AGE) (**Figures S2C** and **S2D**). Third, HSPB1 specifically recognized demixed TDP-43, and could counteract TDP-43 demixing in a concentration-dependent manner (**Figures 2G** and **S2E**). In agreement with the cellular experiments, TDP-43 misfolds and forms aggregates in the demixed phase, which can be prevented by chaperones.

Intra-condensate demixing of TDP-43 also occurred inside lysate stress granules reconstituted by adding recombinant G3BP1 to cellular extract[55] (**Figures S2F–S2H**; see STAR Methods). Therefore, intra-condensate demixing of TDP-43 was observed in three distinct environments: 1) a minimal reconstituted system, 2) cellular extract, and 3) cells. In all cases, TDP-43 partitions into stress granules first, where it then demixes into a TDP-43 enriched phase. The TDP-43 phase undergoes a liquid-to-solid transition and eventually converts into protein aggregates.

Oxidation is a prerequisite for intra-condensate demixing of TDP-43

We next investigated whether environmental insult that triggers protein misfolding is also required for intra-condensate demixing. In our cellular experiments, we used arsenite stress to trigger stress granule assembly, which most likely acts by generating reactive oxygen species (ROS) and causing oxidative stress.[56] Oxidative stress has been implicated in the progression of ALS by triggering TDP-43 aggregation.[28,57,58]

We treated cells with different stressors. The milder oxidant paraquat also induced TDP-43$^{\Delta NLS}$ demixing like arsenite (**Figure S3A**). However, when stress granules were induced without oxidative stress by using puromycin,[59] TDP-43$^{\Delta NLS}$ did not undergo intra-condensate demixing and remained dynamic inside stress granules, even at higher TDP-43 concentrations (**Figures 3A**, **3B** and **S3B**). Additionally, disturbing the protein quality control machinery by inhibiting proteasome or Hsp70 did not trigger TDP-43$^{\Delta NLS}$ demixing in the puromycin-induced stress granules (**Figure S3A**). Thus, oxidative stress is required for TDP-43 demixing and the subsequent generation of aggregates.

To directly investigate the role of oxidation on intra-condensate demixing, we turned to the reconstituted minimal stress granules. When subjected to non-reducing SDS-PAGE, demixed TDP-43 in the reconstituted stress granules formed high-molecular-weight oligomers that could be disassembled

by adding the reducing agent β-mercaptoethanol (β-ME) (**Figure 3C**), revealing the formation of intermolecular disulfide bonds. When reconstituted stress granules were incubated with the oxidizing agent glutathione disulfide (GSSG), TDP-43 demixing was accelerated and occurred at lower threshold concentrations (**Figures 3D**, **3E** and **S3C**). In contrast, the reducing agents β-ME or glutathione (GSH) slowed down TDP-43 demixing, whereas TCEP, a more potent reducing agent, abrogated demixing (**Figures 3D** and **3E**). Importantly, this suggests that TDP-43 is highly sensitive to redox conditions and that background ROS levels are sufficient to drive TDP-43 demixing in test tube experiments with purified proteins.

Taken together, the data from cells and *in vitro* analysis indicate that TDP-43 aggregation requires a double event: 1) up-concentration of TDP-43 by partitioning into stress granules, and 2) demixing coupled to oxidation-driven misfolding of TDP-43 to promote the assembly of protein aggregates.

Hydrophobic patch interactions and disulfide bond formation promote homotypic TDP-43 interactions that govern intra-condensate demixing

To generate molecular hypotheses for the mechanisms governing TDP-43 demixing, we turned to molecular dynamics (MD) simulations. TDP-43 is composed of a folded N-terminal domain (NTD), two tandem folded RNA-recognition motifs (RRM1 and RRM2), and a low-complexity C-terminal domain (CTD) (**Figure 4A**). The CTD contains four sub-regions, one being the hydrophobic patch region (HP, 318–343 aa), which adopts a unique α-helical structure[60–62] (**Figure 4A**).

Considering intra-condensate demixing generates TDP-43 enriched phase in stress granules, we first carried out all-atom MD simulation on TDP-43 condensates to investigate the underlying homotypic interactions (see STAR Methods). Analysis of pairwise, intermolecular contacts within the condensed phase revealed significant interactions from the disordered CTD, especially the HP region (**Figures 4B** and **S4A**), which adopted an α-helical structure consistent with previous NMR studies[63] (**Figure S4B**). Importantly, MD simulation also showed that RRM1, but not RRM2, partially unfolds in the β4–β5 region (**Figures 4C, S4C** and **S4D**) in the condensed phase, leading to solvent exposure of cysteine 173 and 175 (**Figure 4C**). The exposure of these cysteine residues would favor disulfide bond formation, and thereby reduce the

threshold concentration for condensation *via* homotypic TDP-43 interactions, in line with the oxidation requirement for TDP-43 demixing (**Figures 3A** and **3D**).

To test these simulations, we looked at phase separation of purified TDP-43, in the absence of RNA. Deletion of the HP region significantly decreased TDP-43 condensation, while cysteine oxidation by GSSG increased TDP-43 condensation (**Figure 4D**). Thus, HP interactions in the C-terminal domain and disulfide bond formation in RRM1 collectively represent the main homotypic interactions of TDP-43.

We next investigated the relationship between homotypic interactions of TDP-43 and its intra-condensate demixing. Using coarse-grained MD simulations of TDP-43/G3BP1 co-condensates (see STAR Methods), we found that the strength of homotypic interactions of TDP-43, mediated by HP interactions and disulfide bond formation, positively correlates with TDP-43 demixing from G3BP1 (**Figure 4E**).

To test predictions from the simulations, we generated mutants in which either cysteines at position 173 or 175 in RRM1 were replaced with valine or isoleucine (see STAR Methods). MD simulations and NMR analysis showed that the stability of these variants was comparable to wild-type TDP-43 (**Figures S4E** and **S4F**). Cysteine variants also preserved RNA binding similar to wild-type TDP-43 and exhibited normal RNA processing function in cells as revealed by autoregulation[64] (**Figures S4G** and **S4H**). In reconstituted stress granules, both the cysteine variants C173V and C175V showed reduced demixing compared to wild-type TDP-43 (**Figures 4F** and **S4I**). The disease variant M337V, previously shown to strengthen the HP interactions,[65] displayed increased demixing (**Figures 4F** and **S4I**). The ΔHP variant, with significantly reduced demixing in the simulation, could not demix (**Figures 4F** and **S4I**). However, oxidation could trigger the demixing of the ΔHP variant (**Figures 4F** and **S4I**), suggesting a synergy between disulfide bond formation and HP interactions in driving demixing.

We conclude that the interactions mediated by HP interactions and cysteine oxidation in the RRM1 collectively enable TDP-43 phase separation *via* homotypic interactions, thus giving rise to intra-condensate demixing inside stress granules.

355 **TDP-43 aggregation is driven by an α-helix-to-β-sheet transition of the hydrophobic patch region**

Previous work has suggested that irreversible aggregation requires an α-helix to a β-sheet transition of the HP region.[25,26] To test whether this transition is also required for generating pathological aggregates after intra-condensate
360 demixing, we generated an HP variant (HP_{mt5}), in which five mutations were introduced into the HP to destabilize the amyloid cross-β core (PDB: 6n37).[26] Compared to wild-type TDP-43, which gradually forms oligomers over time as assayed by dynamic light scattering (DLS) (**Figure S4J**), HP_{mt5} did not oligomerize (**Figure 4G**). Remarkably, when the HP_{mt5} protein was left in the
365 test tube for 72 h without oligomerization, it continued to form condensates but not aggregates (**Figure S4K**), suggesting that it retains the α-helical structure critical for condensation. In reconstituted stress granules, HP_{mt5} could demix (**Figure 4H**), but the liquid-to-solid transition of the demixed phase was significantly delayed compared to wild-type TDP-43 (**Figure 4I**). This allows us
370 to conclude that intra-condensate demixing and the subsequent liquid-to-solid transition are two distinct steps, with helix-to-sheet transition of the HP region required for aggregation in the demixed TDP-43 phase.

Oxidation-resistant TDP-43 variants with lowered self-assembly propensity abrogate pathological demixing *in vivo*

375 To leverage the insights gleaned from our *in silico* predictions and *in vitro* studies, we engineered TDP-$43^{\Delta NLS}$ variants with altered self-assembly propensities and expressed them in HeLa cells. Supporting the idea that disulfide bond formation and HP interactions synergize to promote TDP-43 demixing, either cysteine mutations or deletion of the HP alone reduced
380 demixing, while the disease mutation M337V enhanced demixing (**Figures 5A** and **S5A**). Importantly, combining the two mutations (denoted as C173V/ΔHP and C175V/ΔHP) abrogated intra-condensate demixing (**Figures 5A** and **5B**). More specifically, although the double mutants were still strongly enriched inside stress granules, they remained dispersed for the time course of the
385 experiment. Consistent with loss of demixing, these variants also did not co-stain with HSPB1 and ubiquitin (**Figures 5C** and **5D**), suggesting that they cannot form pathological aggregates.

ALS is thought to be caused in large parts by a gain of toxicity from persisting protein aggregates.[17,66] To investigate whether intra-condensate demixing leads to aggregates that persist, we followed their stability after stress removal. Of those cells in which G3BP1 condensates dissolved, TDP43$^{\Delta NLS}$ aggregates remained in about 50% of cells (**Figures 5E**, **5F**, and **Video S5**). Importantly, in cells expressing C175V/ΔHP, where intra-condensate demixing was not observed, all cells were able to dissolve TDP-43 assemblies (**Figures 5E**, **5F**, and **Video S6**). We were able to use these assays to distinguish the distinct roles of cysteines and the HP region in forming irreversible aggregates. Variants in which the HP region was deleted (ΔHP) or mutated (HP_{mt5}) significantly reduced recruitment of aggregation markers such as HSPB1 and ubiquitin (**Figures S5B** and **S5C**). After stress removal, they were also dissolved better compared to wild-type and particularly the disease variant M337V (**Figure S5D**). The combined data suggest that although demixing can be driven by disulfide bond formation, stable aggregation requires the helix-to-sheet transition of HP region within demixed condensates. The data further illustrate how pathological aggregates can emerge from dynamic multicomponent condensates and persist even after removal of stress. Such aggregates could be toxic and require specific and energy-intensive mechanisms for their removal.[33]

Intra-condensate demixing results in pathological TDP-43 aggregates in motor neurons, accompanied by disruption of nucleocytoplasmic transport

To assess the pathological relevance of intra-condensate demixing, we expressed TDP-43$^{\Delta NLS}$ in iPSC-derived motor neurons (iPS-MN), a more physiological cell line affected by TDP-43 pathology. Upon arsenite stress, TDP-43$^{\Delta NLS}$ was initially enriched and well dispersed inside stress granules, but later demixed into small puncta (**Figure 6A** and **Video S7**), thus highlighting intra-condensate demixing as a universal phenomenon across different cell lines. In contrast, puromycin was unable to trigger TDP-43 demixing (**Figure 6B**), emphasizing a similar oxidation requirement in motor neurons. Accompanying the demixing process induced by arsenite, TDP-43 dynamics gradually slowed down by FRAP, while TDP-43 stayed dynamic under puromycin stress (**Figure 6C**), indicating hardening during intra-condensate demixing. These demixed puncta co-stained with HSPB1

and exhibited ubiquitination as well (**Figure 6D**). Therefore, intra-condensate demixing generates TDP-43 aggregation with pathological hallmarks in motor neurons.

Impairments in nucleocytoplasmic transport have been associated with pathology in ALS patients.[67,68] We next investigated whether TDP-43 aggregation generated in stress granules causes pathology similar to that observed in patients. TDP-43$^{\Delta NLS}$ aggregates were observed to exhibit interactions with the essential nuclear transport factor importin 2α (**Figure 6E**). Supporting the disturbed nucleocytoplasmic transport, demixed TDP-43$^{\Delta NLS}$ sequestered nuclear wild-type TDP-43 with the intact NLS. Therefore, TDP-43 aggregates in condensates may render toxicity by sequestering key cellular factors.

DISCUSSION

In this work, we have investigated the role of stress granules in generating cytosolic TDP-43 aggregates, which are the most prevalent pathological hallmark of ALS and FTD. The key result of our study is that TDP-43 aggregation in cells requires a double event. One event is the increase in TDP-43 concentration within stress granules that surpasses a critical threshold, and the other is oxidative stress, which increases the tendency of TDP-43 to self-interact. These two events collectively trigger intra-condensate demixing of TDP-43 inside stress granules, and this highly concentrated TDP-43 phase undergoes a liquid-to-solid transition. By uncovering the molecular pathway underlying TDP-43 demixing, we were able to abrogate TDP-43 aggregation in cells. Targeting intra-condensate demixing of TDP-43 within stress granules, as a distinct step on the pathway to aggregation, thus becomes a potential avenue for therapeutic intervention.

Combining our data with previous results allows us to define the role of stress granules in TDP-43 aggregation, which is summarized in Figure 7. Under physiological conditions, TDP-43 is enriched in the nucleus and bound to its RNA targets[16,69] (step 1). However, during oxidative stress, TDP-43 passively leaks into the cytoplasm, where it partitions into stress granules[37] (step 2). Stress granules recruit TDP-43 by providing RNA binding sites, promoting its gradual up-concentration (**Figure 1A**). Once TDP-43 crosses a critical

threshold concentration ($C_{threshold}$) under oxidation conditions, the stress granule condensate formed by a network of heterotypic interactions undergoes intra-condensate demixing (step 3a), giving rise to a separate but initially dynamic TDP-43 phase (step 3b) (**Figures 1B**, **2B** and **6A**). This process is primarily driven by homotypic interactions among TDP-43 molecules mediated by transient, α-helical HP interactions and disulfide bond formation in the RRM1 (step 3c), which disfavors heterotypic interactions of TDP-43 with RNA and promotes homotypic TDP-43 interactions (**Figures 4B, 4C and 4F**). The demixed phase facilitates a liquid-to-solid transition into aggregates exhibiting pathological hallmarks of TDP-43 inclusions (step 4a) (**Figures 1E**, **1F** and **6D**). The aggregation is likely mediated by stable cross-β-sheet interactions from the HP region (step 4b) (**Figures 4H** and **4I**). Further structural work will be required to study the mechanism of aggregation.

Based on cell culture, biochemical assays, MD simulations as well as previously published data, we can build a molecular picture of how homotypic interactions of TDP-43 are favored in the heterotypic environment of stress granules. Raising the local concentration of TDP-43 above a critical threshold by partitioning into stress granules is a prerequisite for the homotypic interactions that drive TDP-43 demixing (**Figures 1A** and **2C**), presumably because it increases the proximity of TDP-43 molecules.[70] Simulations suggest that the interactions are potentiated by two molecular events: One event is partial unfolding of RRM1, which exposes cysteine residues in RRM1 (**Figure 4C**). Oxidative stress, shown to play crucial roles in the progression of various neurodegenerative diseases,[71] increases disulfide bond formation of exposed cysteine residues (**Figures 3A**, **3D** and **6B**). The other event is α-helical interactions between the C-terminal HP region[63] (**Figure 4B**). Indeed, disease mutations within the HP region that favor homotypic interactions can promote TDP-43 demixing (**Figures 4F** and **5A**). The requirement for oxidation and the exacerbation by disease mutations suggest that the intra-condensate demixing of TDP-43 is relevant in the pathogenesis of neurodegenerative diseases.[29,53]

Our data suggest why it has been difficult to pinpoint the trigger for TDP-43 aggregation in cells. Presumably, TDP-43 also misfolds and forms disulfide bonds in the surrounding cytosol under oxidative stress, but the probability for misfolded TDP-43 molecules is not sufficient to trigger homotypic interactions

at physiological concentrations. By locally raising the concentration, intra-condensate demixing within stress granules is required to promote the assembly of persistent pathological TDP-43 aggregates. This is likely because the highly concentrated demixed phase can increase the probability of a helix-to-sheet conversion of the HP region (**Figures 4G–4I**), which eventually facilitate the transition of low-complexity CTD into cross-β-sheet structures.[25,72] These TDP-43 aggregates generated inside stress granules appear to be resistant to removal by the protein quality control machinery, as demonstrated by experiments looking at recovery from stress (**Figure 5F**). We speculate that this may be due to tight cross-β interactions and the formation of an extensive network of disulfide bonds, but this requires additional work in the future.

Multiphasic condensate architectures have been widely described in a cellular context, including nucleoli, nuclear speckles, paraspeckles and P granules.[73–76] The demixed state in multiphasic condensates is fundamentally underpinned by differences in the molecular grammar of individual scaffold molecules governing each phase.[74,77] Presumably these multiphase architectures are additionally dependent upon specific interactions between their diverse set of constituents.[35,78] Here we propose that, in the context of disease, initially well-mixed, multicomponent condensates such as stress granules can similarly undergo a transition into multiphasic condensates, giving rise to a distinct homotypic phase inside a complex heterotypic system that promotes disease emergence.

ACKNOWLEDGMENTS

We would like to acknowledge technical support by E. Geertsma, B. Borgonovo, R. Lemaitre and A. Bogdanova (PEPC facility); A. Pozniakovski and L.D. Mamede (DNA constructs); J. Peychl, and B. Schroth-Diez (light microscopy facility); R. Barsacchi, M. Stöter and C. Möbius (technology development studio); C. Eugster Oegema (organoid and stem cell facility). We would like to thank P. McCall and T. Harmon for discussions on theory. We would like to thank Y. Ye for the help on the cartoon model. We would like to thank A. Karasavvidi for her contributions to confocal microscopy experiments and E.H. Hemamali for performing the RNA binding assays. We would like to thank J. Wang, C. Hoege, A. Fritsch, S. Maharana, J Guillén-Boixet, H. Uechi, A. Majumdar, A. Klosin, L. Hubatsch, A. Pal, M. Ruer-Gruß, J. Savage and D.

525 Sun for critical, as well as very fruitful discussions. We acknowledge funding from the Max Planck Society and the European Research Council (PhaseAge, ERC grant agreement number 725836) to S.A. and A.A.H. Funding from Korber Stiftung to A.A.H. National Institutes of Health (NIH) National Institute for Neurological Disorders and Stroke (NINDS) and National Institute on Aging 530 (NIA) R01 NS114289, and the Department of Defense CDMRP/ALSRP W81XWH-20-1-0241 to Y.M.A.

AUTHOR CONTRIBUTIONS

A.A.H., S.A. and X.Y. designed and coordinated the project. X.Y. planned and co-performed all of the experiments. D.K. planned and performed biochemical 535 experiments and reconstitution assays with initial observation of intra-condensate demixing *in vitro* and its oxidation-dependence. J.N. performed time-resolved confocal microscopy experiments with initial observations of dynamicity, concentration-dependence, and dissolution phenotypes in *vivo*. K.P.-G. performed stimulated emission depletion 540 microscopy with initial observation of intra-condensate demixing *in vivo*. P.M., A.R. and J.M. designed and performed the all-atom MD simulation and Coarse-grained MD simulations. T.M.F and A.S. performed additional biochemical experiments. P.M.P, L.G. and Y.M.A performed RNA binding and TDP-43 autoregulation assay. S.H.W., J.S., H.L.D. and N.L.F. performed NMR 545 experiments to characterize the structure of cysteine variants. A.H. established and provided the STED set-up. A.A.H., S.A., X.Y. and D.K. drafted the manuscript with contributions from other authors. All authors contributed to data analysis and interpretation.

DECLARATION OF INTERESTS

550 A.A.H. is a cofounder of Dewpoint Therapeutics and a member of its scientific advisory board. S.A. is a member of the scientific advisory board of Dewpoint Therapeutics.

FIGURE LEGENDS

Figure 1. TDP-43 undergoes intra-condensate demixing inside stress 555 granules and results in pathological aggregates

(A) Three different cellular phenotypes of TDP-43 in HeLa cells. The cytosolic concentration of TDP-43$^{\Delta NLS}$ in low, medium and high expression cells was measured before stress (top), and TDP-43$^{\Delta NLS}$ concentration inside mCherry-tagged G3BP1 stress granules was measured right before its intra-condensate demixing under stress with 100 μM arsenite (bottom). The cellular and nucleus boundaries are indicated by dashed lines (middle). Scale bar, 10 μm.

(B) The time evolution of a representative stress granule with intra-condensate demixing of TDP-43$^{\Delta NLS}$ in medium expression cells. Stress granules marked by squares under confocal fluorescence microscopy were zoomed in. Scale bar, 10 μm and 1 μm for confocal and zoomed in images, respectively.

(C) Representative STED images of HeLa cells expressing TDP-43$^{\Delta NLS}$ after addition of 100 μM arsenite from 30 min to 120 min. Stress granules marked by squares under confocal microscopy were further visualized by STED microscopy. Scale bar, 10 μm and 500 nm for confocal and STED images, respectively.

(D) FRAP of TDP-43$^{\Delta NLS}$ and mCherry-tagged G3BP1 in medium expression cells after addition of 100 μM arsenite over time. Data represent the mean ± SD.

(E) HSPB1 recognition of TDP-43 aggregates upon intra-condensate demixing by STED. Cells expressing TDP-43$^{\Delta NLS}$ were stressed with 100 μM arsenite and images were acquired before and after demixing. Scale bar, 10 μm and 500 nm for confocal and STED images, respectively.

(F) Ubiquitination of TDP-43 aggregates upon intra-condensate demixing by STED. Cells expressing TDP-43$^{\Delta NLS}$ were stressed with 100 μM arsenite and images were acquired before and after demixing. Scale bar, 10 μm and 500 nm for confocal and STED images, respectively.

(G) mRNA-FISH assay in HeLa cells expressing TDP-43$^{\Delta NLS}$ by STED. Cells expressing TDP-43$^{\Delta NLS}$ were stressed with 100 μM arsenite. Atto647N-labeled oligo-dT oligonucleotides were used to stain poly(A)-containing mRNA. Images were acquired before and after demixing. Scale bar, 10 μm and 500 nm for confocal and STED images, respectively.

See also Figure S1 and Videos S1–S3.

Figure 2. Intra-condensate demixing of TDP-43 promotes a liquid-to-solid phase transition in reconstituted stress granules

(A) TDP-43 recruitment into minimal stress granules. Recombinant G3BP1 (20 μM) and Poly(A) RNA (80 ng/μl) were incubated to form minimal stress granules. TDP-43 WT or ΔRRM1-2 (0.5 μM) was included as a client of stress granules. Scale bar for Figure 2, 10 μm.

(B) Intra-condensate demixing of TDP-43 inside minimal stress granules. TDP-43 (10 μM) was added into minimal stress granules in the presence of 2.5% dextran. Pearson colocalization between G3BP1 and TDP-43 was analyzed by Coloc 2 plugin in Fiji, and 0.85 was set as an apparent demixing threshold. Data represent the mean ± SD.

(C) TDP-43 concentrations in the mixed and demixed phases within minimal stress granules along the intra-condensate demixing process. The time point for demixing is indicated by the dash line.

(D) Representative images of demixed TDP-43 puncta fusion. Puncta undergoing fusion are indicated by white arrowheads.

(E) 3D reconstruction of minimal stress granules upon intra-condensate demixing of TDP-43 at 10 h.

(F) FRAP of TDP-43 in the mixed and demixed phases inside minimal stress granules along the intra-condensate demixing process. Data represent the mean ± SD.

(G) Increasing recognition of demixed TDP-43 by HSPB1 along the intra-condensate demixing process. Alexa 546-labeled HSPB1 (0.5 μM) was added into minimal stress granules and the ratio of fluorescent intensity between HSPB1 and TDP-43 was measured to show the increased stoichiometry and represented as mean ± SD. Representative images of HSPB1 and TDP-43 at 10 h are shown.

See also Figure S2 and Video S4.

Figure 3. Oxidation is a prerequisite for intra-condensate demixing of TDP-43

(A) Oxidization on intra-condensation demixing of TDP-43 in HeLa cells assayed by STED. Cells expressing TDP-43$^{\Delta NLS}$ were treated with 100 μM arsenite or 10 μg/ml puromycin for 120 min. Scale bar, 10 μm and 500 nm for confocal and STED images, respectively.

(B) FRAP of TDP-43$^{\Delta NLS}$ and G3BP1 in stress granules in HeLa cells after addition of 10 μg/ml puromycin for 180 min or 100 μM arsenite for 60 min. Data represent the mean ± SD.

(C) Disulfide bond formation of TDP-43 in minimal stress granules. Stress granules with demixed TDP-43 at 10 h were dissolved with SDS-containing loading buffer and loaded onto SDS-PAGE in the absence or presence of β-ME.

630 (D and E) Redox modifications governing intra-condensate demixing of TDP-43 in minimal stress granules. GSSG (1 mM), β-ME (10 mM), GSH (10 mM) or TCEP (10 mM) were used to treat the stress granules and representative images at 10 h are shown (D). The demixing kinetics, including the demixing time (t_{demix}) and correlation coefficient at 10 h (R_{10h}), were 635 quantified (E). Data represent the mean ± SD. Scale bar, 10 μm.

See also Figure S3.

Figure 4. Hydrophobic patch interactions and disulfide bond formation constitute homotypic TDP-43 interactions that govern intra-condensate demixing

640 (A) Schematic of folded and disordered regions in TDP-43 (1–414 aa). NTD, N-terminal domain (1–80 aa); RRM1 and RRM2, RNA recognition motif 1 (106–176 aa) and 2 (191–262 aa); CTD, C-terminal domain (263–414 aa); G, glycine-rich (274–314 aa); HP, hydrophobic patch region (318–343 aa); Q/N, Q and N-rich (344–365 aa); S, serine-rich (370–402 aa). Point mutations 645 studied in the following sections are also shown here.

(B) Representative snapshot from an atomistic MD simulation (3 μs) of a full-length TDP-43 condensate composed of 25 chains using a slab-geometry setup (left), close-up of two interacting TDP-43 chains within the condensate (middle) and the corresponding two-dimensional, intermolecular contact map 650 showing pairwise, residue-level interactions (right). In the contact map, contact propensity for a specific residue refers to the average number of contacts ($\langle N_{ij} \rangle$) per frame of the trajectory summated over the pairwise contributions of all TDP-43 chains and normalized by the total number of chains (n=25).

(C) Structures of folded (PDB: 4IUF) and partially unfolded RRM1 domain in 655 simulation of the TDP-43 condensed phase (top), and comparison between per-residue root-mean-square fluctuation (RMSF) for RRM1 in the dilute and condensed phases (bottom). The RRM1 domains are shown in ribbon representation with cysteine residues (173/175) shown as sticks. RMSF analysis for each residue, which is used to quantify the local flexibility of 660 proteins, was computed over three independent trajectories for the monomer

in the dilute phase (4.5 μs each) and over 25 chains in the condensed phase (2.5 μs each), respectively. Data represent the mean ± SD.

(D) The HP interactions and disulfide bond formation favor TDP-43 condensation. Phase separation of TDP-43 WT or ΔHP with titrated concentrations in the absence or presence of GSSG (5 mM) are shown. Relative droplet fraction of TDP-43 versus the total protein concentration is quantified and shown as mean ± SD. Scale bar, 10 μm.

(E) Cross-section of TDP-43/G3BP1 droplet snapshots (left) and protein concentration ratio (C_{G3BP1}/C_{TDP-43}) at the droplet center obtained from the simulations (right). The droplets comprised of an equal number of TDP-43 and G3BP1 chains (25 each). Simulation was computed over 5 blocks of 1–1.1 μs duration after excluding the initial 2 μs as equilibration. A ratio of 1 corresponds to a well-mixed droplet while values approaching 0 indicate strong demixing. Data represent the mean ± SEM.

(F) Intra-condensate demixing of TDP-43 variants (10 μM) in minimal stress granules. Pearson colocalization between G3BP1 and TDP-43 was analyzed and the demixing time (t_{demix}) is shown. Data represent the mean ± SD.

(G) DLS assay for TDP-43 HP_{mt5}. The mutated residues are shown based on the cryo-EM structure of the TDP-43 amyloid cross-β core (PDB: 6n37). HP_{mt5} (80 μM) was incubated in 500 mM KCl. At the time indicated, samples (5 μM) were assayed by DLS. Data represented as the mean ± SD.

(H) Intra-condensate demixing of TDP-43 HP_{mt5} in minimal stress granules. HP_{mt5} (10 μM) was added into minimal stress granules. Pearson colocalization between G3BP1 and TDP-43 was analyzed. Data represent the mean ± SD. Scale bar, 10 μm.

(I) FRAP assay for mobile fractions of TDP-43 WT and HP_{mt5} within the demixed phase along intra-condensate demixing in minimal stress granules. Data represent the mean ± SD.

See also Figure S4.

Figure 5. Oxidation-resistant TDP-43 variants with lowered self-assembly propensity abrogate pathological demixing *in vivo*

(A) Pearson colocalization between G3BP1 and TDP-$43^{\Delta NLS}$ variants under 100 μM arsenite stress for 120 min.

(B) Representative STED images of HeLa cells expressing TDP-$43^{\Delta NLS}$ variants after addition of 100 μM arsenite for 120 min. Stress granules marked

by squares under confocal microscopy were further visualized by STED microscopy. Scale bar, 10 μm and 500 nm for confocal and STED images, respectively.

(C and D) Prevention of intra-condensate demixing of TDP-43 abolishing the formation of pathological aggregates. Cells expressing TDP-43$^{\Delta NLS}$ variants were stressed with 100 μM arsenite for 120 min and images were acquired for HSPB1 (C) and ubiquitin (D) by confocal microscopy. Stress granules marked by squares were zoomed in. Scale bar, 10 μm and 5 μm for confocal and zoomed in images, respectively.

(E) Quantification of dissolution of TDP-43$^{\Delta NLS}$ aggregates. HeLa cells expressing TDP-43$^{\Delta NLS}$ variants were stressed with 100 μM arsenite for 60 min following 120 min recovery. The demixed TDP-43$^{\Delta NLS}$ aggregates were monitored in cells capable of dissolving stress granules, and data were presented as the fraction of these cells able to dissolve TDP-43$^{\Delta NLS}$ aggregates. Data represent the mean ± SD.

(F) Live imaging of cells expressing TDP-43$^{\Delta NLS}$ variants during stress with 100 μM arsenite for 60 min and recovery for 120 min. Stress granules marked by squares were zoomed in. Scale bar, 10 μm and 1 μm for fluorescent and zoomed in images, respectively.

See also Figure S5, Videos S5 and S6.

Figure 6. Intra-condensate demixing results in pathological aggregates in motor neurons, accompanied by impairment of nucleocytoplasmic transport

(A) Representative images of intra-condensate demixing of TDP-43$^{\Delta NLS}$ in iPS-MN. The cells were cotransfected with GFP-tagged TDP-43$^{\Delta NLS}$ and mCherry-tagged G3BP1 and live-cell imaging was performed after addition of 100 μM arsenite. Scale bar, 10 μm and 5 μm for whole-cell and zoomed in images, respectively.

(B) Oxidization on intra-condensation demixing of TDP-43 in iPS-MN cells. Motor neurons expressing TDP-43$^{\Delta NLS}$ were treated with 10 μg/ml puromycin or 100 μM arsenite for 60 min. Normalized fluorescent intensities for TDP-43 and stress granules along the straight line are shown. Scale bar, 10 μm and 2 μm for confocal and zoomed in images, respectively.

(C) FRAP of TDP-43$^{\Delta NLS}$ in stress granules in iPS-MN cells after addition of 100 μM arsenite or 10 μg/ml puromycin for 60 min. Data represent the mean ± SD.

(D) TDP-43 demixing generating pathological aggregates. Motor neurons expressing TDP-43$^{\Delta NLS}$ were stressed with 100 μM arsenite for 90 min, and images were acquired for HSPB1 or ubiquitin staining by confocal microscopy. Normalized fluorescent intensities for each channel along the straight line are shown. Scale bar, 2 μm.

(E) TDP-43 aggregation impairing nucleocytoplasmic transport in iPS-MN. Motor neurons expressing TDP-43$^{\Delta NLS}$ alone or TDP-43$^{\Delta NLS}$ together with TDP-43-myc with intact NLS were stressed with 100 μM arsenite for 90 min, and images were acquired for importin-α or TDP-43-myc staining by confocal microscopy. Normalized fluorescent intensities for each channel along the straight line are shown. Scale bar, 2 μm.

See also Video S7.

Figure 7. Model of intra-condensate demixing of TDP-43 inside stress granules generating pathological aggregates

The intra-condensate demixing of TDP-43 inside stress granules generating pathological aggregates at different scales, from cells to condensates to molecular basis, is shown schematically. Intra-condensate demixing of TDP-43 occurs by up-concentration inside stress granules under oxidation (step 3a). The demixed but dynamic TDP-43 phase facilitates a liquid-to-solid transition into pathological aggregates (steps 3b and 4a). See Discussion for details.

SUPPLEMENTAL FIGURE LEGENDS

Figure S1. Intra-condensate demixing and aggregate formation of TDP-43 *in vivo*, related to Figure 1

(A) Fluorescent intensity curve of recombinant GFP-tagged TDP-43 at different concentrations.

(B) Representative images of HeLa cells with low, medium and high expression of TDP-43$^{\Delta NLS}$ before stress during live-cell imaging. High-contrast images are also shown to highlight the low and medium expression cells. The cellular and nucleus boundaries are indicated by dashed lines. Arrow heads indicate small puncta prior to stress in high expression cells. Scale bar, 10 μm.

(C) FRAP of TDP-43$^{\Delta NLS}$ and G3BP1 in stress granules in low expression cells after addition of 100 μM arsenite for 60 min. Data represent the mean ± SD.

765 (D) FRAP of TDP-43$^{\Delta NLS}$ puncta (G3BP1-negative) in high expression cells before stress and after addition of 100 μM arsenite for 60 min. Data represent the mean ± SD.

(E) Representative confocal images of HeLa cells expressing wild-type TDP-43 with intact NLS after addition of 100 μM arsenite for 120 min. Scale

770 bar, 10 μm and 5 μm for confocal and zoomed in images, respectively.

(F) Representative images of demixed TDP-43$^{\Delta NLS}$ puncta fusion during live-cell imaging. Puncta undergoing fusion are indicated by white arrowheads. Scale bars, 5 μm.

(G) TDP-43$^{\Delta NLS}$ concentrations in HeLa cells in the cytosol before stress

775 (cytosolic), in stress granules at the beginning of demixing (stress granule) and in demixed TDP-43$^{\Delta NLS}$ puncta at the end of demixing (demixed).

(H) Phosphorylation of TDP-43$^{\Delta NLS}$ aggregation upon intra-condensate demixing by confocal microscopy. Cells expressing TDP-43$^{\Delta NLS}$ were stressed with 100 μM arsenite and images were acquired before and after demixing.

780 Scale bar, 10 μm and 5 μm for confocal and zoomed in images, respectively.

(I) Cytoplasmic TDP-43$^{\Delta NLS}$ aggregates generated from intra-condenste demixing recruiting nuclear TDP-43 by confocal microscopy. Cells cotransfected with GFP-tagged TDP-43$^{\Delta NLS}$ (100 ng) and Myc-tagged TDP-43 (50 ng) with intact NLS were stressed with 100 μM arsenite for 120 min. Scale

785 bar, 10 μm and 5 μm for confocal and zoomed in images, respectively.

Figure S2. Intra-condensate demixing and aggregate formation of TDP-43 in reconstituted stress granules, related to Figure 2

(A) Reduced RNA binding by TDP-43 upon intra-condensate demixing in minimal stress granules at 10 h. The TDP-43-rich phase contains less RNA

790 stained by BoBo-3 dye (1 μM) than the G3BP1-rich phase. Scale bar for Figure S2, 10 μm.

(B) Representative condensates in minimal stress granules at 10 h are shown before and after bleaching. The sites of bleaching for mixed and demixed phases are indicated by red solid and white dashed circles, respectively.

795 (C) The increasing amytracker staining of demixed TDP-43 along intra-condensate demixing process. Amyloid-specific dye amytracker (2.5 μM) was added into minimal stress granules and the ratio of fluorescent intensity

between amytracker and TDP-43 was measured to show the increasing stoichiometry. Data represent the mean ± SD.

(D) TDP-43 aggregation in minimal stress granules by SDD-AGE assay. Stress granules containing TDP-43 (10 μM) at 1 h and 10 h were dissolved by 0.3% sarkosyl and analyzed by SDD-AGE containing 0.3% sarkosyl. TDP-43 monomer and oligomer are indicated accordingly.

(E) Prevention of TDP-43 demixing by HSPB1 in minimal stress granules. The experiment was carried out with titrated concentrations of HSPB1 and representative images at 10 h are shown.

(F) TDP-43 recruitment into reconstituted lysate stress granules. Recombinant G3BP1 (20 μM) and lysate from HeLa cells containing ~2 μg/μl cellular proteins were incubated to form reconstituted lysate stress granules. TDP-43 WT or ΔRRM1-2 (0.5 μM) was included as a client of stress granules.

(G) Intra-condensate demixing of TDP-43 in lysate stress granules. TDP-43 (10 μM) was added into lysate stress granules in the presence of 2.5% dextran.

(H) FRAP of TDP-43 in reconstituted lysate stress granules as in (G) over time. The bleaching sites upon recovery are indicated by white dashed circles. Data represent the mean ± SD.

Figure S3. Oxidation is required for intra-condensate demixing of TDP-43, related to Figure 3

(A) Effects of different stressors on intra-condensation demixing of TDP-43$^{\Delta NLS}$ in HeLa cells by confocal microscopy. Cells expressing TDP-43$^{\Delta NLS}$ were treated with paraquat alone (5 mM) for oxidation, VER-155008 (10 μM) for Hsp70 inhibition or MG132 (10 μM) for proteasome inhibition in the presence of puromycin (10 μg/ml) for 120 min. Scale bar, 10 μm and 5 μm for confocal and zoomed in images, respectively.

(B) TDP-43$^{\Delta NLS}$ concentrations inside stress granules after addition of puromycin (10 μg/ml) in HeLa cells for 180 min.

(C) The threshold concentration for intra-condensate demixing of TDP-43 in minimal stress granules in the absence or presence of GSSG (1 mM).

Figure S4. Homotypic interactions mediated by HP interactions and disulfide bond formation govern TDP-43 demixing, related to Figure 4

(A) One-dimensional contact map showing per-residue interaction probabilities which were computed through the summation of all pairwise interactions for each residue position from the two-dimensional contact map in Figure 4B.

(B) Comparison of per-residue α-helix fraction for CTD of TDP-43 (267–414 aa) between MD simulations in condensed phase and solution NMR. α-helix fractions were computed based on DSSP secondary structure definitions for MD simulations over 25 chains for the 2.5 μs trajectory, and secondary chemical shifts using the delta-2D program for NMR. Data represent the mean ± SEM.

(C) dRMSD of C_α atoms as a function of time with respect to the initial conformation (t=0) for RRM1 (left) and RRM2 (right). Stable RRM domains (dRMSD<0.4 nm) are shown in light gray while unstable domains (dRMSD>0.4 nm) are colored differently.

(D) Comparison between per-residue RMSF for RRM2 domain in the dilute and condensed phase from atomistic MD simulations. The mean RMSF was computed over three independent trajectories (4.5 μs each) for the dilute phase (monomer) and 25 chains (2.5 μs each) for the condensed phase, respectively. Data represent the mean ± SD.

(E) Conformational stability of RRM1 cysteine variants in comparison to the wild-type based on RMSF analysis at 300 K. RMSF for each residue was calculated over three independent trajectories (2.0 μs each, excluding the first 500 ns). Data represent the mean ± SD.

(F) ^{1}H-^{15}N heteronuclear single quantum coherence (HSQC) spectra of wild-type RRM1-2 (102–269 aa, black) and RRM1-2 C173V/C175I (orange) (left). The spectra were recorded at 298 K using 500 μM protein in 50 mM KPi buffer (pH 6.8) and 150 mM NaCl. Chemical shift assignments were transferred from the BMRB deposited data (BMRB ID: 27613). The chemical shift perturbations of C173V/C175I are mapped on wild-type RRM1-2 (PDB: 4BS2), and 173/175 residues are highlighted in spheres (right). Colors are assigned according to ^{1}H and ^{15}N changes in residues, with ^{1}H >0.05 ppm and ^{15}N >0.1 ppm in magenta, ^{1}H <0.05 ppm and ^{15}N <0.1 ppm in light blue, and residues without substantial change in orange, respectively.

(G) Affinity of TDP-43 variants for $A(GU)_6$ RNA, determined by fluorescence anisotropy. FITC-labeled RNA (5 nM) was added into series diluted TDP-43 in Tris buffer (pH 8.0) containing 150 mM NaCl.

(H) Autoregulation function of TDP-43 in cells. HEK293 cell lines stably expressing HA-tagged wild-type TDP-43 or C173V/C175I upon tetracycline induction for 72 h. Ratio of endogenous TARDBP mRNA and TDP-43 protein between the presence (TC+) and the absence of induction (TC-) are shown, respectively. Data represent the mean ± SD.

(I) Intra-condensate demixing assay for TDP-43 variants. TDP-43 variants (10 μM) were added into the minimal stress granules formed by recombinant G3BP1 (20 μM) and Poly(A) RNA (80 ng/μl) in the presence of 2.5% dextran. Scale bar, 10 μm.

(J) TDP-43 oligomer formation by DLS assay. Wild-type TDP-43 (80 μM) was incubated in 500 mM KCl at 25°C. At the time indicated, aliquots of the samples were diluted into 5 μM in 500 mM KCl and assayed by DLS. Data represent the mean ± SD.

(K) TDP-43 HP_{mt5} maintaining droplet formation. Wild-type TDP-43 or HP_{mt5} (80 μM) was incubated in 500 mM KCl. After 72 h, samples were diluted into a final concentration of 10 μM in 75 mM KCl. Scale bar, 10 μm.

Figure S5. TDP-43 variants with oxidation-resistance and lowered self-assembly propensity abrogate demixing and aggregation *in vivo*, related to Figure 5

(A) Intra-condensate demixing of TDP-43 variants in HeLa cells by STED. Cells expressing TDP-$43^{\Delta NLS}$ variants were stressed with 100 μM arsenite for 120 min and images were taken by STED microscopy. The cellular and nucleus boundaries are indicated by dashed lines. Scale bar, 10 μm and 500 nm for confocal and STED images, respectively.

(B and C) The HP region interactions contributing to TDP-43 aggregation in the demixed phase. Cells expressing TDP-$43^{\Delta NLS}$ variants were stressed with 100 μM arsenite for 60 min, and the ratio of fluorescent intensity between HSPB1 (B) or ubiquitin (C) and demixed TDP-$43^{\Delta NLS}$ was quantified.

(D) Quantification of dissolution of TDP-$43^{\Delta NLS}$ aggregates. HeLa cells expressing TDP-$43^{\Delta NLS}$ variants were stressed with 100 μM arsenite for 60 min following 120 min recovery. The demixed TDP-$43^{\Delta NLS}$ aggregates were monitored in cells capable of dissolving stress granules, and data were presented as the fraction of these cells able to dissolve TDP-$43^{\Delta NLS}$ aggregates. Data represent the mean ± SD.

STAR METHODS

RESOURCE AVAILABILITY

Lead contact

Further information and requests for resources and reagents should be directed to and will be fulfilled by the lead contact, Anthony A. Hyman (hyman@mpi-cbg.de).

Materials availability

This study did not generate new unique reagents.

Data and code availability

- Data reported in this paper will be shared by the lead contact upon request.
- This paper does not report original code.
- Any additional information required to reanalyze the data reported in this paper is available from the lead contact upon request.

EXPERIMENTAL MODEL AND STUDY PARTICIPANT DETAILS

Strains for plasmid and protein preparation

E. coli DH5α (ThermoFisher) was used for plasmid cloning. *E. coli* BL21 (DE3) (Stratagene) was used for TDP-43 RRM1-2 expression in NMR assay. *E. coli* was cultured at 37°C.

Cell lines and cell culture

HeLa Kyoto (female), HEK293 Flp-In™ T-REX™ (Thermo Fisher) and human induced pluripotent stem cells (WTC-11) were used in this study. The parental HeLa Kyoto line was authenticated. Generation of HeLa BAC-G3BP1-mCherry line was described before.[79] The stable HEK293 HA-TDP-43 line was generated by co-transfection of pcDNA5/FRT/TO/HA-TDP-43 and pOG44 (Invitrogen) using lipofectamine 3000 (Invitrogen) into HEK293 Flp-In™ T-REx™ (ThermoFisher). Following transfection, cells were selected with 75 µg/ml hygromycin (Sigma). Healthy control iPS line (WTC-11) was obtained from the Coriell Institute *via* the Organoid and Stem Cell Facility at MPI-CBG, Dresden.

930 All cells were grown in humidified incubators at 37°C and 5% CO_2. HeLa cells were cultured in DMEM high glucose (4.5 g/l) media (Gibco) supplemented with 10% fetal bovine serum (Gibco), 100 units/ml penicillin and 100 µg/ml streptomycin (Gibco). HeLa BAC-G3BP1-mCherry and HEK293 HA-TDP-43 cells were additionally maintained in the presence of 5 µg/ml blasticidin (Gibco)
935 and 75 µg/ml hygromycin, respectively. iPS cells were maintained in mTeSR1 media (StemCell Technologies) on geltrex-coated dishes (ThermoFisher Scientific). They were passaged using ReLeSR (StemCell Technologies) in the presence of 5 µM ROCK-inhibitor (Y-27632, Abcam).

METHOD DETAILS

940 **Plasmid and protein preparation**

TDP-43 variants with point mutations were generated by site-directed mutagenesis, while sequences with deletions were ordered from IDT and constructed into pOEM1 (Mirus Bio), pET28b(+) (Merck), pcDNA5™/FRT/TO (Thermo Fisher), pcDNA3.1 (Invitrogen) or pCW57.1 (RRID: Addgene_41393)
945 vectors. All constructs were confirmed by DNA sequencing.

TDP-43-GFP variants and G3BP1-SNAP were expressed in sf9 insect cells (BioTrend) and purified as described previously.[34,80] In brief, sf9 cells expressing TDP-43 or G3BP1 in 500 ml culture were collected and applied to His-tag column and then superdex 200 column for purification. SUMO-TDP-43
950 variants were expressed in *E. coli* BL21 (DE3) and purified as previously described.[81] Protein concentrations were measured spectrophotometrically at 280 nm. See below for information on protein production for NMR studies.

Motor neuron differentiation and transfection

iPS cells were grown to ~80% confluency before initiation of differentiation.
955 The differentiation protocol was described previously,[82] with some modifications. On day 1, embroid body formation was initiated. Cells were pre-incubated with ROCK-inhibitor (5 µM) and subsequently dissociated using TrypLE Express (Gibco) to a single-cell suspension. The cells were collected in differentiation media consisting of 0.5×N2 supplement, 0.5×B27 plus
960 supplement in DMEM-F12 with GlutaMAX:Neurobasal plus (1:1, all Gibco). The differentiation media was supplemented with ROCK-inhibitor (5 µM), LDN-193189 (500 nM, Peprotech), SB-431542 (30 µM, Peprotech),

CHIR-99021 (3 μM, Tocris) and ascorbic acid (200 μM, Sigma-Aldrich). Cells in 6-cm non-adherent dishes were placed on an orbital shaker inside the incubator at 60 rpm overnight.

On day 2, embryoid bodies formed, and media was exchanged for identical media. On day 3, and every day subsequently, media was exchanged for differentiation media supplemented with retinoic acid (200 nM, Sigma-Aldrich), smoothened agonist (SAG, 500 nM, Peprotech) and ascorbic acid (200 μM). On day 10, the embryoid bodies (containing motor neuron progenitors at this stage) were pre-incubated for 1 h with ROCK-inhibitor (5 μM) and dissociated with TrypLE Express to single cells. These were cryopreserved in differentiation media supplemented with 10% DMSO and ROCK-inhibitor (5 μM).

For transfection experiments, motor neuron progenitors were thawed and plated at 50 K cells/cm^2 into 8-well polymer-bottom slides (Ibidi), coated with poly-L-ornithine (0.003%, Sigma-Aldrich) and laminin (5 μg/ml, Sigma-Aldrich). Progenitors were plated in differentiation media supplemented with ROCK-inhibitor (5 μM), CHIR-99021 (3 μM), retinoic acid (200 nM), SAG (500 nM) and EGF (25 ng/ml, Peprotech). This media allowed the progenitors to continue expanding before transfection. After 48 h, the cells were transfected with plasmids expressing doxycycline-inducible TDP-43$^{\Delta NLS}$-GFP (100 ng) and G3BP1-mCherry (100 ng) using lipofectamine STEM (ThermoFisher Scientific). After an additional 24 h, media was exchanged to terminal differentiation medium (1×B27 plus supplement in Neurobasal plus), supplemented with DAPT (10 μM, Cell Signaling), BDNF (10 ng/ml, Peprotech) and GDNF (10 ng/ml, Peprotech). After 7 days, expression of fluorescent constructs was induced by addition of doxycycline (2 μM, Sigma-Aldrich).

Cell transfection and stress treatment

HeLa cells were seeded into a 96-well plate (Greiner) or 8-well polymer-bottom slides (Ibidi). After 48 h of seeding, plasmids expressing TDP-43 variants (100 ng for 96-well and 150 ng for 8-well) were transfected using lipofectamine 3000. For the stressed conditions, sodium arsenite (100 μM, Fisher Chemical), puromycin (10 μg/ml, Sigma), paraquat (5 mM, Sigma-Aldrich), VER-155008 (10 μM, Sigma-Aldrich) or MG132 (10 μM, MedChemExpress) was added to

cells after 24 h of transfection. iPSC-derived motor neurons were stressed by 100 μM sodium arsenite at 24 h after induction of fluorescent constructs.

Immunofluorescence staining

Cultured cells were fixed with 4% formaldehyde (w/v) (Thermo Scientific) in PBS for 10 min at room temperature. Fixed samples were permeabilized in 0.1% Triton X-100/PBS for 10 min at room temperature. Samples were blocked using 0.2% fish gelatin (Sigma) in PBS for 1 h at room temperature, followed by incubation with primary antibodies and fluorescent-labeled secondary antibodies in blocking solution for 1 h at room temperature. Nuclei were stained with DAPI (ThermoFisher). Samples were stored at 4°C until imaging.

The following primary antibodies were used for immunofluorescent staining: Rabbit anti-G3BP1 (ThermoFisher), Mouse anti-HSPB1 (Enzo Life Sciences), Mouse anti-Importin alpha 2 (Novus Biologicals), Mouse anti-Ubiquitin (Sigma-Aldrich), Mouse Anti-TDP-43 phospho Ser409/410 (Cosmobio), FluoTag-Q anti-GFP AbberiorStar580 (NanoTag Biotechnologies), and Mouse anti-Myc (Santa Cruz). The following secondary antibodies were used: Goat anti-rabbit Alexa Fluor 594 (Invitrogen), Goat anti-mouse Alexa Fluor 647 (Invitrogen), and Goat anti-rabbit STAR RED (Abberior).

mRNA-FISH

mRNA-FISH assay was performed as previously described with modifications.[83] HeLa cells transfected with TDP-43$^{\Delta NLS}$ were fixed with 4% formaldehyde in PBS for 10 min at room temperature, followed by washing with PBS-FISH buffer (PBS containing 0.2 mg/ml RNase-free BSA). The fixed samples were treated with permeabilization buffer (0.2% Tween 20 in PBS) for 15 min at room temperature, followed by washing twice with hybridization wash buffer (2×saline-sodium citrate, 10% formamide and 0.2 mg/ml BSA). The Atto647N-labeled oligo-dT_{25} probe (IDT) was prepared to 2.5 ng/ul in hybridization buffer (10% dextran sulfate, 2×saline-sodium citrate, 10% formamide, 1 mg/ml tRNA and 0.2 mg/ml BSA), and the stain was carried out at 37°C for 12 h. After FISH staining, immunostaining was performed in PBS-based buffers afterward.

TDP-43 autoregulation assay

TDP-43 autoregulation assay was carried out as described previously.[84] HEK293 HA-TDP-43 cells were induced with tetracycline (1 μg/ml, Sigma-Aldrich) to express HA-TDP-43 for 72 h. Non-treated cells were used as control. Half of the cells were used for immunoblotting analysis of endogenous and transgenic TDP-43 and the other half for mRNA quantification. Immunoblots were probed with TDP-43 antibody (Proteintech) and GAPDH (Proteintech) as loading control. TRIzol reagent (ThermoFisher) and M-MLV reverse transcriptase (ThermoFisher) were used for RNA extraction and cDNA production according to the manufacturer's instructions, respectively.

Reconstituted minimal stress granules

Minimal stress granules were induced by addition of G3BP1-SNAP (20 μM, 5% labeled with SNAP-Surface Alexa Fluor 647 (New England Biolabs)) to poly(A) RNA (80 ng/μl, Sigma) in PIPES buffer (20 mM PIPES/KOH pH 7.4, 100 mM KCl and 2.5% w/v dextran). TDP-43 variants were added into the reactions and images were taken in 384-well microplates (Perkin Elmer) at indicated time. RNA was visualized employing BOBO-3 dimeric cyanine dye (5 μM, Invitrogen), where indicated. For aggregation assay in this system, HSPB1 or amytracker 680 (2.5 μM, Ebba Biotech) was added, where indicated. TDP-43 demixing was analyzed with Pearson colocalization between G3BP1 and TDP-43 by Coloc 2 plugin in Fiji.

Formation of lysate stress granules

The high-fidelity reconstitution of stress granules in mammalian cellular lysate was carried out as previously described with modifications.[55] HeLa cells were grown to confluency in 10-cm dishes (Corning). Cell pellets were lysed in 250 μl of lysis buffer (50 mM Tris-HCl pH 7.0, 0.5% Tergitol type NP-40, 1×protease inhibitor cocktail III (Merck), 2.5% Murine RNase inhibitor (NEB)). After centrifugation at 21 000 g at 20°C for 5 min, lysate supernatants containing ~2 μg/μl cellular proteins were mixed with purified G3BP1-SNAP (20 μM, 5% labeled with Alexa Fluor 647) to form reconstituted lysate stress granules in Tris buffer (50 mM Tris-HCl pH 7.0, 100 mM KCl, and 2.5% w/v dextran). TDP-43 (10 μM) was added into the reactions and images were taken in 384-well microplates at indicated time.

Phase separation and droplet fraction assay

For analysis of phase separation, GFP-tagged TDP-43 variants were diluted into titrated concentrations in 20 mM PIPES/KOH (pH 7.4) and 75 mM KCl. The samples (20 µl) were added into 384-well medium binding plates (Greiner Bio-One) and incubated for 1 h before taking images by confocal microscopy. The relative droplet fraction of TDP-43 was quantified as described previously.[80] In brief, we used microscopy to measure the fluorescence intensity in the condensed and dilute phase and determined the protein amount inside and outside of condensates. The software Fiji was used for the segmentation and fluorescence intensity assay.

Image acquisition (Microscopy)

For the in *vitro* assay, images were taken using an Andor STORM Spinning disc microscope with an Andor Neo sCMOS/Andor Clara CCD camera and a Plan Apo 60×1.2 water-immersion objective (Nikon). For fixed cell samples, the images were collected by a Yokogawa CV7000 high-content spinning disk confocal microscope with a 60×1.2 NA water-immersion objective.

For live-cell timelapse imaging, cells were imaged on a widefield inverted Olympus IX71 microscope using 60×1.2 NA water-immersion or 60×1.42 NA oil-immersion Plan-Apochromat objectives, a sCMOS camera (pco.edge 5.5) and a DeltaVision control unit (AppliedPrecision). While on the microscope, cells were maintained at 37°C and 5% CO_2. Timelapses were typically 60–120 minutes with imaging every 1–2 minutes.

Images were analyzed using Fiji software. Assessing demixing status in live-cell imaging was conducted manually. Stress granule-independent demixing was defined as the stress-induced formation of TDP-43$^{\Delta NLS}$ positive puncta without any overlap or adjacency to G3BP1-positive stress granules. Intra-condensate demixing was defined as TDP-43$^{\Delta NLS}$ puncta inside or in contact with stress granules. Cytosolic and intra-stress granule intensities of TDP-43$^{\Delta NLS}$ were measured in single-plane images at time points right before adding arsenite and emergence of demixed puncta, respectively.

Stimulated emission depletion microscopy (STED)

For STED, cells were imaged using an Abberior 2 Color-STED system (Abberior Instruments) with a 100×1.35 NA silicon objective (Olympus). AbberiorStar 580 (Abberior) and StarRed 635 (Abberior) were imaged with a pulsed laser at 560 and 640 nm, respectively, in combination with a 775 nm,

40 MHz pulsed depletion laser (Katana HP, 3W, 1 ns pulse duration, NKT Photonics). Imspector imaging software (Abberior Instruments) was used for STED microscopy. The optimal combination of excitation intensity, STED power and pixel dwell time were established by minimizing the onset of strong photo bleaching. Postprocessing was done using the Matlab software. To reduce high frequency noise, STED images were mildly deconvolved using the Richardson-Lucy algorithm. The PSF was approximated by a 2D Gaussian with a FWHM that was determined from independent bead measurements at the respective STED power. To avoid deconvolution artifacts, we used a low number of 6 iterations. Using these conditions, we saw a significant improvement in the signal-to-noise ratio, but little to no change in resolution. Images were analyzed using Fiji plug in Coloc2, to calculate the Pearson colocalization correlation.

Fluorescence recovery after photobleaching (FRAP)

FRAP experiments for *in vitro* samples were carried out with an Andor STORM Spinning disc microscope equipped with a FRAPPA unit and a Plan Apo 60×1.2 water-immersion objective. Bleaching was performed using a 488 nm DPSS laser at 100% intensity in five repeats with a dwell time of 20 µs. Images before and after photobleaching were recorded in a single focal plane. The Fiji software was used for image analysis.

For live-cell FRAP experiments, cells were imaged on either an inverted Zeiss LSM780 or LSM880 point-scanning laser confocal microscope with GaAsP detectors, using a 40×1.2 NA C-Apochromat water-immersion objective. Cells were maintained at 37°C and 5% CO_2 during the experiments. GFP for TDP-43$^{\Delta NLS}$ and mCherry for G3BP1 signals were bleached using defined regions around individual stress granules with 488 nm and 594 nm laser wavelengths, respectively. The Fiji software was used for image analysis. The average intensity of 3 of pre-bleaching frames was normalized to 100%, and intensity of the first frame after bleaching was normalized to 0%.

NMR spectroscopy

TDP-43 RRM1-2 variants (102-269 aa) were expressed in media containing $^{15}NH_4Cl$ and purified as described previously.[85] NMR experiments were performed at 298 K on a Bruker Avance 850 MHz 1H Larmor frequency spectrometer with an HCN TCI z-gradient cryoprobe. The spectra were

1130 recorded using 500 μM protein in 50 mM KPi buffer (pH 6.8), 150 mM NaCl, 1 mM DTT and 5% (v/v) D_2O. Chemical shift assignments were transferred from BMRB deposited data (BMRB ID:27613).[86] The NMR data were processed with Bruker Topspin and analyzed using CCPNMR.[87]

Dynamic light scattering (DLS)

1135 TDP-43 (80 μM) was incubated in 20 mM PIPES/KOH (pH 7.4) and 500 mM KCl at 25°C. At the time indicated, aliquots of the samples were diluted into 5 μM and assayed by DLS. DLS assays for TDP-43 oligomerization were performed using a Zetasizer Nano ZSP (Malvern Panalytical). The samples (15 μl) in a precision quartz cuvette were illuminated by a 632 nm laser, and 1140 the intensity of light with 173° forward scattering was recorded for 2 min with 5 s autocorrelations.

Fluorescence anisotropy assay

Fluorescence anisotropy binding assay was performed as described previously.[84] FITC-labeled $A(GU)_6$ RNA (5 nM, IDT) was added into a series of 1145 diluted TDP-43 variants (0–200 nM) in 10 mM Tris buffer (pH 8.0) containing 150 mM NaCl, 5% glycerol, 5% sucrose and 1mM TCEP. The anisotropy measurements were performed using a Spectra Max i3 plate reader (Molecular Devices) with excitation and emission at 480 nm and 520 nm, respectively.

1150 **SDD-AGE assay**

Semi-denaturing detergent agarose gel electrophoresis (SDD-AGE) was used to detect TDP-43 oligomerization and aggregation in minimal stress granules. Samples were incubated in SDD-AGE sample buffer (20 mM PIPES pH 7.4, 8% glycerol, 0.3% sarkosyl (Sigma-Aldrich) and bromophenol blue) and 1155 analyzed on 1.5% agarose gel with 0.3% sarkosyl detergent. The protein on the gel was transferred to nitrocellulose membrane (Invitrogen) for western blot assay, and GFP-tagged TDP-43 was detected by the primary Goat anti-EGFP (in house) and secondary Donkey anti-goat IRDye 800CW (LI-COR Biosciences) antibodies.

1160 **All-atom MD simulations**

Initial structures and molecular modeling

All systems were simulated in explicit solvent and modeled using the AMBER99SBws-STQ force field and TIP4P/2005 water model with improved

salt parameters.[88–91] The initial structure for isolated RRM1 domain was extracted from a crystallographic structure (PDB: 4IUF, chain A).[92] Cysteine mutants were introduced in the RRM1 domain based on the Dunbrack rotamer library in ChimeraX (UCSF). The full-length TDP-43 model used for monomer and coarse-grained simulations was built based on the available structures of N-terminal domain (PDB: 5MRG),[93] RRM1-2 (PDB: 4BS2)[85] and C-terminal domain (PDB: 2N3X) using the MOE program.[94]

TDP-43 condensate system was generated using the steps detailed in a previous study.[95] Briefly, the initial configuration for simulating the all-atom condensate phase was obtained from a coarse-grained simulation of TDP-43 (25 chains) using the HPS-Urry coarse-grained model,[96] which ran for 5 μs. The final configuration of the coarse-grained simulation was converted into an atomistic representation using MODELLER (UCSF) based on the structures of the N-terminal domain (PDB: 5MRG) and RRM1-2 (PDB: 4BS2) and then minimized using the CAMPARI Monte Carlo engine and the implicit solvent ABSINTH force field.[97]

Simulation protocol

RRM1 and TDP-43 monomer were solvated in octahedral boxes of 6.0 nm and 15.0 nm length, respectively. TDP-43 condensate system was solvated with ions in a box with dimensions of 11.9×11.9×45 nm^3. The solvated, electroneutral protein systems were subjected to energy minimization performed *via* the steepest descent algorithm using GROMACS-2020.[98] After minimization, 100–150 mM NaCl was added to mimic physiological salt concentration, and additional counterions were included to ensure electroneutrality. For temperature equilibration, the Nosé-Hoover thermostat with a coupling constant of 1 ps was used for protein, water and ions, with a fixed temperature of 300 K.[99] For TDP-43 monomer, the NVT equilibration (100 ps) was followed by NPT equilibration (100 ps) using the Berendsen barostat with isotropic coupling and a 5 ps coupling constant for pressure control.[100] For the TDP-43 condensate, NVT equilibration (100 ns) was followed by NPT equilibration (100 ns) using the Berendsen barostat. Following the equilibration steps, production runs were performed using the Langevin Middle Integrator (friction coefficient = 1 ps^{-1}) in OpenMM-7.7.[101,102] Runs were performed in the NVT ensemble (TDP-43 monomer) and NPT ensemble (TDP-43 condensate) at 300 K. For the NPT ensemble, the pressure

was fixed at 1 bar with the Monte Carlo Membrane Barostat. The membrane barostat was isotropic in the x and y dimensions, with a free z dimension.

For both equilibration and production runs, short-range nonbonded interactions were calculated using a cutoff radius of 0.9 nm, while long-range electrostatics were handled with the PME method.[103] To enable a timestep of 4 fs, the hydrogen mass was increased by 1.5 times, and hydrogen-containing bonds were constrained using the SHAKE algorithm.[104]

Analysis

The intermolecular contact map from the condensed phase trajectory was computed using in house python scripts. For calculation of the intermolecular contact map, two residues were considered to form a contact if any two heavy atoms of the residues were within 6 Å of each other. For a specific residue pair, the average number of contacts ($<N_{ij}>$) per trajectory frame was summated over pairwise contributions from all 25 chains. The contact propensity is defined as $<N_{ij}>$ normalized by the total number of chains (=25) and calculated over the last microsecond of the trajectory. All other analyses were performed using GROMACS analysis tools. The secondary structure fractions were calculated based on the DSSP library using the gmx do_dssp program.[105] The per-residue root mean-square fluctuation (RMSF) and distance root mean square deviation (dRMSD) were computed using gmx rmsf and gmx rmsdist, respectively. The structural snapshots were generated using UCSF ChimeraX.

Coarse-Grained MD simulation

The coarse-grained droplet simulations of TDP-43 and G3BP1 were performed using the HOOMD-Blue 2.9.7 software package with additional features incorporated using AZ plugins (version 0.10.1; https://github.com/mphowardlab/azplugins).[106] The folded domains in both proteins were constrained as a rigid body, and the initial configuration was prepared based on the HPS-Urry model.[96] The simulations were run for 7–7.5 μs in the NVT ensemble at 325 K with a time step of 10 fs. The Langevin thermostat was used for temperature control, with a friction factor, $\gamma = m_{AA}/\tau$. Here, m_{AA} is the mass of each amino acid bead, τ is the damping factor, which was set to 1000 ps. In the HP model, an interaction strength (ϵ) of 0.2 kcal/mol was set between all residues, while in the HPHP model, ϵ was set to 0.4 kcal/mol for residues within HP to allow stronger HP-HP interactions. In the

SS model with disulfide bond formation, a harmonic bond with k_b = 20 kcal mol^{-1} $Å^{-2}$ and r_0 = 3.0 Å was added between RRM1 pairs at C173 position to mimic disulfide bonds between RRM1 domains. For density calculations, the first 2 μs of the simulation were considered as an equilibration period and excluded from subsequent calculations. Radial densities were computed using the method described in our previous work.[107]

Design of RRM1 cysteine variants

To design the mutations for cysteines at positions 173 and 175, we performed sequence and structural alignments of TDP-43 RRM1 and RRM2 using Clustal Omega and ChimeraX, respectively. For structural alignment, the structures of RRM1 and RRM2 were obtained from the RCSB Protein Data Bank (PDB:4IUF for RRM1, PDB:4BS2 for RRM2). Based on both alignments, we generated mutants in which either cysteines at position 173 or 175 in RRM1 were replaced with the corresponding valine (position 255) or isoleucine (position 257) in RRM2.

QUANTIFICATION AND STATISTICAL ANALYSIS

Statistical analysis was performed in Excel and Origin 2021b on data acquired from at least three independent experiments. Matched samples were compared using two-tailed Student's paired t-test, in which n.s. (*p*-value>0.05), * (0.01<*p*-value≤ 0.05), ** (0.001<*p*-value≤ 0.01) and *** (*p*-value≤ 0.001).

SUPPLEMENTAL VIDEO LEGENDS

Video S1. Low expression of TDP-43$^{\Delta NLS}$ dispersed inside stress granules in HeLa cells, related to Figure 1

HeLa cells with low expression of TDP-43$^{\Delta NLS}$ were stressed by addition of 100 μM arsenite. TDP-43$^{\Delta NLS}$ (green) and stress granules marked by mCherry-tagged G3BP1 (magenta) were visualized. Scale bar, 10 μm.

Video S2. High expression of TDP-43$^{\Delta NLS}$ forming aggregates independent of stress granules in HeLa cells, related to Figure 1

HeLa cells with high expression of TDP-43$^{\Delta NLS}$ were stressed by addition of 100 μM arsenite. TDP-43$^{\Delta NLS}$ (green) and stress granules marked by mCherry-tagged G3BP1 (magenta) were visualized. Scale bar, 10 μm.

Video S3. Medium expression of TDP-43$^{\Delta NLS}$ undergoing intra-condensate demixing inside stress granules in HeLa cells, related to Figure 1

HeLa cells with medium expression of TDP-43$^{\Delta NLS}$ were stressed by addition of 100 μM arsenite. TDP-43$^{\Delta NLS}$ (green) and stress granules marked by mCherry-tagged G3BP1 (magenta) were visualized. Scale bar, 10 μm.

Video S4. Intra-condensate demixing of TDP-43 inside minimal stress granules, related to Figure 2

TDP-43 (10 μM) was added into minimal stress granules formed by G3BP1 (20 μM) and Poly(A) RNA (80 ng/μl) in the presence of 2.5% dextran. TDP-43 (green) and G3BP1 (magenta) were visualized. Scale bar, 10 μm.

Video S5. Dissolution assay of demixed TDP-43$^{\Delta NLS}$ aggregates in HeLa cells, related to Figure 5

HeLa BAC-G3BP1-mCherry cells with medium expression of TDP-43$^{\Delta NLS}$ were stressed by addition of 100 μM arsenite for 60 min and recovery for 120 min. TDP-43$^{\Delta NLS}$ (green) and stress granules marked by mCherry-tagged G3BP1 (magenta) were visualized. Scale bar, 10 μm.

Video S6. Dissolution assay of TDP-43$^{\Delta NLS}$ C175V/ΔHP inside stress granules in HeLa cells, related to Figure 5

HeLa BAC-G3BP1-mCherry cells with medium expression of TDP-43$^{\Delta NLS}$ C175V/ΔHP were stressed by addition of 100 μM arsenite for 60 min and recovery for 120 min. TDP-43$^{\Delta NLS}$ C175V/ΔHP (green) and stress granules marked by mCherry-tagged G3BP1 (magenta) were visualized. Scale bar, 10 μm.

Video S7. Intra-condensate demixing of TDP-43$^{\Delta NLS}$ inside stress granules in iPS-MN cells, related to Figure 6

iPS-MN cells cotransfected with TDP-43$^{\Delta NLS}$ and G3BP1 were stressed by addition of 100 μM arsenite. TDP-43$^{\Delta NLS}$ (green) and stress granules marked by mCherry-tagged G3BP1 (magenta) were visualized. Scale bar, 10 μm.

1295 **REFERENCES**

1. Iqbal, K., Liu, F., Gong, C.-X., and Grundke-Iqbal, I. (2010). Tau in Alzheimer disease and related tauopathies. Curr. Alzheimer Res. *7*, 656–664. 10.2174/156720510793611592.

2. Bartels, T., Choi, J.G., and Selkoe, D.J. (2011). α-Synuclein occurs
1300 physiologically as a helically folded tetramer that resists aggregation. Nature *477*, 107–110. 10.1038/nature10324.

3. Ciryam, P., Tartaglia, G.G., Morimoto, R.I., Dobson, C.M., and Vendruscolo, M. (2013). Widespread aggregation and neurodegenerative diseases are associated with supersaturated
1305 proteins. Cell Rep. *5*, 781–790. 10.1016/j.celrep.2013.09.043.

4. Cosacak, M.I., Bhattarai, P., Bocova, L., Dzewas, T., Mashkaryan, V., Papadimitriou, C., Brandt, K., Hollak, H., Antos, C.L., and Kizil, C. (2017). Human TAUP301L overexpression results in TAU hyperphosphorylation without neurofibrillary tangles in adult zebrafish brain. Sci. Rep. *7*, 12959.
1310 10.1038/s41598-017-13311-5.

5. Guo, J.L., Buist, A., Soares, A., Callaerts, K., Calafate, S., Stevenaert, F., Daniels, J.P., Zoll, B.E., Crowe, A., Brunden, K.R., et al. (2016). The Dynamics and Turnover of Tau Aggregates in Cultured Cells: INSIGHTS INTO THERAPIES FOR TAUOPATHIES. J. Biol. Chem. *291*,
1315 13175–13193. 10.1074/jbc.M115.712083.

6. Erustes, A.G., Stefani, F.Y., Terashima, J.Y., Stilhano, R.S., Monteforte, P.T., da Silva Pereira, G.J., Han, S.W., Calgarotto, A.K., Hsu, Y.-T., Ureshino, R.P., et al. (2018). Overexpression of α-synuclein in an astrocyte cell line promotes autophagy inhibition and apoptosis. J.
1320 Neurosci. Res. *96*, 160–171. 10.1002/jnr.24092.

7. Bido, S., Muggeo, S., Massimino, L., Marzi, M.J., Giannelli, S.G., Melacini, E., Nannoni, M., Gambarè, D., Bellini, E., Ordazzo, G., et al. (2021). Microglia-specific overexpression of α-synuclein leads to severe dopaminergic neurodegeneration by phagocytic exhaustion and
1325 oxidative toxicity. Nat. Commun. *12*, 6237. 10.1038/s41467-021-26519-x.

8. Altman, T., Ionescu, A., Ibraheem, A., Priesmann, D., Gradus-Pery, T., Farberov, L., Alexandra, G., Shelestovich, N., Dafinca, R., Shomron, N., et al. (2021). Axonal TDP-43 condensates drive neuromuscular junction disruption through inhibition of local synthesis of nuclear encoded mitochondrial proteins. Nat. Commun. *12*, 6914. 10.1038/s41467-021-27221-8.

9. Buratti, E., and Baralle, F.E. (2001). Characterization and functional implications of the RNA binding properties of nuclear factor TDP-43, a novel splicing regulator of CFTR exon 9. J. Biol. Chem. *276*, 36337–36343. 10.1074/jbc.M104236200.

10. Freibaum, B.D., Chitta, R.K., High, A.A., and Taylor, J.P. (2010). Global analysis of TDP-43 interacting proteins reveals strong association with RNA splicing and translation machinery. J. Proteome Res. *9*, 1104–1120. 10.1021/pr901076y.

11. Polymenidou, M., Lagier-Tourenne, C., Hutt, K.R., Huelga, S.C., Moran, J., Liang, T.Y., Ling, S.-C., Sun, E., Wancewicz, E., Mazur, C., et al. (2011). Long pre-mRNA depletion and RNA missplicing contribute to neuronal vulnerability from loss of TDP-43. Nat. Neurosci. *14*, 459–468. 10.1038/nn.2779.

12. Ayala, Y.M., Zago, P., D'Ambrogio, A., Xu, Y.-F., Petrucelli, L., Buratti, E., and Baralle, F.E. (2008). Structural determinants of the cellular localization and shuttling of TDP-43. J. Cell Sci. *121*, 3778–3785. 10.1242/jcs.038950.

13. Tziortzouda, P., Van Den Bosch, L., and Hirth, F. (2021). Triad of TDP43 control in neurodegeneration: autoregulation, localization and aggregation. Nat. Rev. Neurosci. *22*, 197–208. 10.1038/s41583-021-00431-1.

14. Pinarbasi, E.S., Cağatay, T., Fung, H.Y.J., Li, Y.C., Chook, Y.M., and Thomas, P.J. (2018). Active nuclear import and passive nuclear export are the primary determinants of TDP-43 localization. Sci. Rep. *8*, 7083. 10.1038/s41598-018-25008-4.

15. Neumann, M., Sampathu, D.M., Kwong, L.K., Truax, A.C., Micsenyi, M.C., Chou, T.T., Bruce, J., Schuck, T., Grossman, M., Clark, C.M., et al.

1360 (2006). Ubiquitinated TDP-43 in frontotemporal lobar degeneration and amyotrophic lateral sclerosis. Science *314*, 130–133. 10.1126/science.1134108.

16. Ling, S.-C., Polymenidou, M., and Cleveland, D.W. (2013). Converging mechanisms in ALS and FTD: disrupted RNA and protein homeostasis.
1365 Neuron *79*, 416–438. 10.1016/j.neuron.2013.07.033.

17. Prasad, A., Bharathi, V., Sivalingam, V., Girdhar, A., and Patel, B.K. (2019). Molecular Mechanisms of TDP-43 Misfolding and Pathology in Amyotrophic Lateral Sclerosis. Front. Mol. Neurosci. *12*, 25. 10.3389/fnmol.2019.00025.

1370 18. Josephs, K.A., Murray, M.E., Whitwell, J.L., Parisi, J.E., Petrucelli, L., Jack, C.R., Petersen, R.C., and Dickson, D.W. (2014). Staging TDP-43 pathology in Alzheimer's disease. Acta Neuropathol. *127*, 441–450. 10.1007/s00401-013-1211-9.

19. Nelson, P.T., Dickson, D.W., Trojanowski, J.Q., Jack, C.R., Boyle, P.A.,
1375 Arfanakis, K., Rademakers, R., Alafuzoff, I., Attems, J., Brayne, C., et al. (2019). Limbic-predominant age-related TDP-43 encephalopathy (LATE): consensus working group report. Brain *142*, 1503–1527. 10.1093/brain/awz099.

20. Sun, Y., and Chakrabartty, A. (2017). Phase to Phase with TDP-43.
1380 Biochemistry *56*, 809–823. 10.1021/acs.biochem.6b01088.

21. Sun, X., Song, J., Huang, H., Chen, H., and Qian, K. (2018). Modeling hallmark pathology using motor neurons derived from the family and sporadic amyotrophic lateral sclerosis patient-specific iPS cells. Stem Cell Res. Ther. *9*, 315. 10.1186/s13287-018-1048-1.

1385 22. Cascella, R., Capitini, C., Fani, G., Dobson, C.M., Cecchi, C., and Chiti, F. (2016). Quantification of the Relative Contributions of Loss-of-function and Gain-of-function Mechanisms in TAR DNA-binding Protein 43 (TDP-43) Proteinopathies. J. Biol. Chem. *291*, 19437–19448. 10.1074/jbc.M116.737726.

1390 23. Hartl, F.U. (2017). Protein Misfolding Diseases. Annu. Rev. Biochem. *86*, 21–26. 10.1146/annurev-biochem-061516-044518.

24. Gasset-Rosa, F., Lu, S., Yu, H., Chen, C., Melamed, Z., Guo, L., Shorter, J., Da Cruz, S., and Cleveland, D.W. (2019). Cytoplasmic TDP-43 De-mixing Independent of Stress Granules Drives Inhibition of Nuclear Import, Loss of Nuclear TDP-43, and Cell Death. Neuron *102*, 339-357.e7. 10.1016/j.neuron.2019.02.038.

25. Arseni, D., Chen, R., Murzin, A.G., Peak-Chew, S.Y., Garringer, H.J., Newell, K.L., Kametani, F., Robinson, A.C., Vidal, R., Ghetti, B., et al. (2023). TDP-43 forms amyloid filaments with a distinct fold in type A FTLD-TDP. Nature *620*, 898–903. 10.1038/s41586-023-06405-w.

26. Cao, Q., Boyer, D.R., Sawaya, M.R., Ge, P., and Eisenberg, D.S. (2019). Cryo-EM structures of four polymorphic TDP-43 amyloid cores. Nat. Struct. Mol. Biol. *26*, 619–627. 10.1038/s41594-019-0248-4.

27. Johnson, B.S., Snead, D., Lee, J.J., McCaffery, J.M., Shorter, J., and Gitler, A.D. (2009). TDP-43 is intrinsically aggregation-prone, and amyotrophic lateral sclerosis-linked mutations accelerate aggregation and increase toxicity. J. Biol. Chem. *284*, 20329–20339. 10.1074/jbc.M109.010264.

28. Cohen, T.J., Hwang, A.W., Unger, T., Trojanowski, J.Q., and Lee, V.M.Y. (2012). Redox signalling directly regulates TDP-43 via cysteine oxidation and disulphide cross-linking. EMBO J. *31*, 1241–1252. 10.1038/emboj.2011.471.

29. Alberti, S., and Hyman, A.A. (2021). Biomolecular condensates at the nexus of cellular stress, protein aggregation disease and ageing. Nat. Rev. Mol. Cell Biol. *22*, 196–213. 10.1038/s41580-020-00326-6.

30. Dormann, D., Rodde, R., Edbauer, D., Bentmann, E., Fischer, I., Hruscha, A., Than, M.E., Mackenzie, I.R.A., Capell, A., Schmid, B., et al. (2010). ALS-associated fused in sarcoma (FUS) mutations disrupt Transportin-mediated nuclear import. EMBO J. *29*, 2841–2857. 10.1038/emboj.2010.143.

31. Li, Y.R., King, O.D., Shorter, J., and Gitler, A.D. (2013). Stress granules as crucibles of ALS pathogenesis. J. Cell Biol. *201*, 361–372. 10.1083/jcb.201302044.

32. Nedelsky, N.B., and Taylor, J.P. (2019). Bridging biophysics and

1425 neurology: aberrant phase transitions in neurodegenerative disease. Nat. Rev. Neurol. *15*, 272–286. 10.1038/s41582-019-0157-5.

33. Hipp, M.S., Kasturi, P., and Hartl, F.U. (2019). The proteostasis network and its decline in ageing. Nat. Rev. Mol. Cell Biol. *20*, 421–435. 10.1038/s41580-019-0101-y.

1430 34. Guillén-Boixet, J., Kopach, A., Holehouse, A.S., Wittmann, S., Jahnel, M., Schlüßler, R., Kim, K., Trussina, I.R.E.A., Wang, J., Mateju, D., et al. (2020). RNA-Induced Conformational Switching and Clustering of G3BP Drive Stress Granule Assembly by Condensation. Cell *181*, 346-361.e17. 10.1016/j.cell.2020.03.049.

1435 35. Sanders, D.W., Kedersha, N., Lee, D.S.W., Strom, A.R., Drake, V., Riback, J.A., Bracha, D., Eeftens, J.M., Iwanicki, A., Wang, A., et al. (2020). Competing Protein-RNA Interaction Networks Control Multiphase Intracellular Organization. Cell *181*, 306-324.e28. 10.1016/j.cell.2020.03.050.

1440 36. Yang, P., Mathieu, C., Kolaitis, R.-M., Zhang, P., Messing, J., Yurtsever, U., Yang, Z., Wu, J., Li, Y., Pan, Q., et al. (2020). G3BP1 Is a Tunable Switch that Triggers Phase Separation to Assemble Stress Granules. Cell *181*, 325-345.e28. 10.1016/j.cell.2020.03.046.

37. Liu-Yesucevitz, L., Bilgutay, A., Zhang, Y.-J., Vanderweyde, T., Citro, A.,
1445 Mehta, T., Zaarur, N., McKee, A., Bowser, R., Sherman, M., et al. (2010). Tar DNA binding protein-43 (TDP-43) associates with stress granules: analysis of cultured cells and pathological brain tissue. PLoS One *5*, e13250. 10.1371/journal.pone.0013250.

38. Colombrita, C., Zennaro, E., Fallini, C., Weber, M., Sommacal, A.,
1450 Buratti, E., Silani, V., and Ratti, A. (2009). TDP-43 is recruited to stress granules in conditions of oxidative insult. J. Neurochem. *111*, 1051–1061. 10.1111/j.1471-4159.2009.06383.x.

39. McGurk, L., Lee, V.M., Trojanowksi, J.Q., Van Deerlin, V.M., Lee, E.B., and Bonini, N.M. (2014). Poly-A binding protein-1 localization to a subset
1455 of TDP-43 inclusions in amyotrophic lateral sclerosis occurs more frequently in patients harboring an expansion in C9orf72. J. Neuropathol. Exp. Neurol. *73*, 837–845. 10.1097/NEN.0000000000000102.

40. Mori, F., Yasui, H., Miki, Y., Kon, T., Arai, A., Kurotaki, H., Tomiyama, M., and Wakabayashi, K. (2023). Colocalization of TDP-43 and stress granules at the early stage of TDP-43 aggregation in amyotrophic lateral sclerosis. Brain Pathol., e13215. 10.1111/bpa.13215.

41. McGurk, L., Gomes, E., Guo, L., Mojsilovic-Petrovic, J., Tran, V., Kalb, R.G., Shorter, J., and Bonini, N.M. (2018). Poly(ADP-Ribose) Prevents Pathological Phase Separation of TDP-43 by Promoting Liquid Demixing and Stress Granule Localization. Mol. Cell *71*, 703-717.e9. 10.1016/j.molcel.2018.07.002.

42. Chen, Y., and Cohen, T.J. (2019). Aggregation of the nucleic acid-binding protein TDP-43 occurs via distinct routes that are coordinated with stress granule formation. J. Biol. Chem. *294*, 3696–3706. 10.1074/jbc.RA118.006351.

43. Streit, L., Kuhn, T., Vomhof, T., Bopp, V., Ludolph, A.C., Weishaupt, J.H., Gebhardt, J.C.M., Michaelis, J., and Danzer, K.M. (2022). Stress induced TDP-43 mobility loss independent of stress granules. Nat. Commun. *13*, 5480. 10.1038/s41467-022-32939-0.

44. Mann, J.R., Gleixner, A.M., Mauna, J.C., Gomes, E., DeChellis-Marks, M.R., Needham, P.G., Copley, K.E., Hurtle, B., Portz, B., Pyles, N.J., et al. (2019). RNA Binding Antagonizes Neurotoxic Phase Transitions of TDP-43. Neuron *102*, 321-338.e8. 10.1016/j.neuron.2019.01.048.

45. Hans, F., Glasebach, H., and Kahle, P.J. (2020). Multiple distinct pathways lead to hyperubiquitylated insoluble TDP-43 protein independent of its translocation into stress granules. J. Biol. Chem. *295*, 673–689. 10.1074/jbc.RA119.010617.

46. Lu, S., Hu, J., Arogundade, O.A., Goginashvili, A., Vazquez-Sanchez, S., Diedrich, J.K., Gu, J., Blum, J., Oung, S., Ye, Q., et al. (2022). Heat-shock chaperone HSPB1 regulates cytoplasmic TDP-43 phase separation and liquid-to-gel transition. Nat. Cell Biol. *24*, 1378–1393. 10.1038/s41556-022-00988-8.

47. Winton, M.J., Igaz, L.M., Wong, M.M., Kwong, L.K., Trojanowski, J.Q., and Lee, V.M.-Y. (2008). Disturbance of nuclear and cytoplasmic TAR DNA-binding protein (TDP-43) induces disease-like redistribution,

sequestration, and aggregate formation. J. Biol. Chem. *283*, 13302–13309. 10.1074/jbc.M800342200.

48. Kulak, N.A., Pichler, G., Paron, I., Nagaraj, N., and Mann, M. (2014). Minimal, encapsulated proteomic-sample processing applied to copy-number estimation in eukaryotic cells. Nat. Methods *11*, 319–324. 10.1038/nmeth.2834.

49. Patrick M. McCall, Kyoohyun Kim, Anatol W. Fritsch, J.M. Iglesias-Artola, L.M. Jawerth, Jie Wang, M. Ruer, J. Peychl, Andrey Poznyakovskiy, Jochen Guck, et al. (2020). Quantitative phase microscopy enables precise and efficient determination of biomolecular condensate composition. BioRxiv.

50. Neumann, M., Kwong, L.K., Truax, A.C., Vanmassenhove, B., Kretzschmar, H.A., Van Deerlin, V.M., Clark, C.M., Grossman, M., Miller, B.L., Trojanowski, J.Q., et al. (2007). TDP-43-positive white matter pathology in frontotemporal lobar degeneration with ubiquitin-positive inclusions. J. Neuropathol. Exp. Neurol. *66*, 177–183. 10.1097/01.jnen.0000248554.45456.58.

51. Hasegawa, M., Arai, T., Nonaka, T., Kametani, F., Yoshida, M., Hashizume, Y., Beach, T.G., Buratti, E., Baralle, F., Morita, M., et al. (2008). Phosphorylated TDP-43 in frontotemporal lobar degeneration and amyotrophic lateral sclerosis. Ann. Neurol. *64*, 60–70. 10.1002/ana.21425.

52. Alami, N.H., Smith, R.B., Carrasco, M.A., Williams, L.A., Winborn, C.S., Han, S.S.W., Kiskinis, E., Winborn, B., Freibaum, B.D., Kanagaraj, A., et al. (2014). Axonal transport of TDP-43 mRNA granules is impaired by ALS-causing mutations. Neuron *81*, 536–543. 10.1016/j.neuron.2013.12.018.

53. Mathieu, C., Pappu, R. V, and Taylor, J.P. (2020). Beyond aggregation: Pathological phase transitions in neurodegenerative disease. Science *370*, 56–60. 10.1126/science.abb8032.

54. Taylor, J.P., Brown, R.H., and Cleveland, D.W. (2016). Decoding ALS: from genes to mechanism. Nature *539*, 197–206. 10.1038/nature20413.

55. Freibaum, B.D., Messing, J., Yang, P., Kim, H.J., and Taylor, J.P. (2021).

High-fidelity reconstitution of stress granules and nucleoli in mammalian cellular lysate. J. Cell Biol. *220*. 10.1083/jcb.202009079.

56. Bernstam, L., and Nriagu, J. (2000). Molecular aspects of arsenic stress. J. Toxicol. Environ. Health. B. Crit. Rev. *3*, 293–322. 10.1080/109374000436355.

57. Buratti, E. (2018). TDP-43 post-translational modifications in health and disease. Expert Opin. Ther. Targets *22*, 279–293. 10.1080/14728222.2018.1439923.

58. Valle, C., and Carrì, M.T. (2017). Cysteine Modifications in the Pathogenesis of ALS. Front. Mol. Neurosci. *10*, 5. 10.3389/fnmol.2017.00005.

59. Aulas, A., Fay, M.M., Szaflarski, W., Kedersha, N., Anderson, P., and Ivanov, P. (2017). Methods to Classify Cytoplasmic Foci as Mammalian Stress Granules. J. Vis. Exp. 10.3791/55656.

60. Conicella, A.E., Zerze, G.H., Mittal, J., and Fawzi, N.L. (2016). ALS Mutations Disrupt Phase Separation Mediated by α-Helical Structure in the TDP-43 Low-Complexity C-Terminal Domain. Structure *24*, 1537–1549. 10.1016/j.str.2016.07.007.

61. Lim, L., Wei, Y., Lu, Y., and Song, J. (2016). ALS-Causing Mutations Significantly Perturb the Self-Assembly and Interaction with Nucleic Acid of the Intrinsically Disordered Prion-Like Domain of TDP-43. PLoS Biol. *14*, e1002338. 10.1371/journal.pbio.1002338.

62. Jiang, L.-L., Che, M.-X., Zhao, J., Zhou, C.-J., Xie, M.-Y., Li, H.-Y., He, J.-H., and Hu, H.-Y. (2013). Structural transformation of the amyloidogenic core region of TDP-43 protein initiates its aggregation and cytoplasmic inclusion. J. Biol. Chem. *288*, 19614–19624. 10.1074/jbc.M113.463828.

63. Conicella, A.E., Dignon, G.L., Zerze, G.H., Schmidt, H.B., D'Ordine, A.M., Kim, Y.C., Rohatgi, R., Ayala, Y.M., Mittal, J., and Fawzi, N.L. (2020). TDP-43 α-helical structure tunes liquid-liquid phase separation and function. Proc. Natl. Acad. Sci. U. S. A. *117*, 5883–5894. 10.1073/pnas.1912055117.

64. Ayala, Y.M., De Conti, L., Avendaño-Vázquez, S.E., Dhir, A., Romano, M., D'Ambrogio, A., Tollervey, J., Ule, J., Baralle, M., Buratti, E., et al. (2011). TDP-43 regulates its mRNA levels through a negative feedback loop. EMBO J. *30*, 277–288. 10.1038/emboj.2010.310.

65. Ervilha Pereira, P., Schuermans, N., Meylemans, A., LeBlanc, P., Versluys, L., Copley, K.E., Rubien, J.D., Altheimer, C., Peetermans, M., Debackere, E., et al. (2023). C-terminal frameshift variant of TDP-43 with pronounced aggregation-propensity causes rimmed vacuole myopathy but not ALS/FTD. Acta Neuropathol. *145*, 793–814. 10.1007/s00401-023-02565-1.

66. Lee, E.B., Lee, V.M.-Y., and Trojanowski, J.Q. (2011). Gains or losses: molecular mechanisms of TDP43-mediated neurodegeneration. Nat. Rev. Neurosci. *13*, 38–50. 10.1038/nrn3121.

67. Chou, C.-C., Zhang, Y., Umoh, M.E., Vaughan, S.W., Lorenzini, I., Liu, F., Sayegh, M., Donlin-Asp, P.G., Chen, Y.H., Duong, D.M., et al. (2018). TDP-43 pathology disrupts nuclear pore complexes and nucleocytoplasmic transport in ALS/FTD. Nat. Neurosci. *21*, 228–239. 10.1038/s41593-017-0047-3.

68. Ditsworth, D., Maldonado, M., McAlonis-Downes, M., Sun, S., Seelman, A., Drenner, K., Arnold, E., Ling, S.-C., Pizzo, D., Ravits, J., et al. (2017). Mutant TDP-43 within motor neurons drives disease onset but not progression in amyotrophic lateral sclerosis. Acta Neuropathol. *133*, 907–922. 10.1007/s00401-017-1698-6.

69. Hallegger, M., Chakrabarti, A.M., Lee, F.C.Y., Lee, B.L., Amalietti, A.G., Odeh, H.M., Copley, K.E., Rubien, J.D., Portz, B., Kuret, K., et al. (2021). TDP-43 condensation properties specify its RNA-binding and regulatory repertoire. Cell *184*, 4680-4696.e22. 10.1016/j.cell.2021.07.018.

70. Mohanty, P., Rizuan, A., Kim, Y.C., Fawzi, N.L., and Mittal, J. (2023). A complex network of interdomain interactions underlies the conformational ensemble of monomeric TDP-43 and modulates its phase behavior. Protein Sci., e4891. 10.1002/pro.4891.

71. Barnham, K.J., Masters, C.L., and Bush, A.I. (2004). Neurodegenerative diseases and oxidative stress. Nat. Rev. Drug Discov. *3*, 205–214.

10.1038/nrd1330.

1590 72. Arseni, D., Hasegawa, M., Murzin, A.G., Kametani, F., Arai, M., Yoshida, M., and Ryskeldi-Falcon, B. (2022). Structure of pathological TDP-43 filaments from ALS with FTLD. Nature *601*, 139–143. 10.1038/s41586-021-04199-3.

73. West, J.A., Mito, M., Kurosaka, S., Takumi, T., Tanegashima, C., Chujo,
1595 T., Yanaka, K., Kingston, R.E., Hirose, T., Bond, C., et al. (2016). Structural, super-resolution microscopy analysis of paraspeckle nuclear body organization. J. Cell Biol. *214*, 817–830. 10.1083/jcb.201601071.

74. Feric, M., Vaidya, N., Harmon, T.S., Mitrea, D.M., Zhu, L., Richardson, T.M., Kriwacki, R.W., Pappu, R. V, and Brangwynne, C.P. (2016).
1600 Coexisting Liquid Phases Underlie Nucleolar Subcompartments. Cell *165*, 1686–1697. 10.1016/j.cell.2016.04.047.

75. Fei, J., Jadaliha, M., Harmon, T.S., Li, I.T.S., Hua, B., Hao, Q., Holehouse, A.S., Reyer, M., Sun, Q., Freier, S.M., et al. (2017). Quantitative analysis of multilayer organization of proteins and RNA in
1605 nuclear speckles at super resolution. J. Cell Sci. *130*, 4180–4192. 10.1242/jcs.206854.

76. Folkmann, A.W., Putnam, A., Lee, C.F., and Seydoux, G. (2021). Regulation of biomolecular condensates by interfacial protein clusters. Science *373*, 1218–1224. 10.1126/science.abg7071.

1610 77. Kaur, T., Raju, M., Alshareedah, I., Davis, R.B., Potoyan, D.A., and Banerjee, P.R. (2021). Sequence-encoded and composition-dependent protein-RNA interactions control multiphasic condensate morphologies. Nat. Commun. *12*, 872. 10.1038/s41467-021-21089-4.

78. Musacchio, A. (2022). On the role of phase separation in the biogenesis
1615 of membraneless compartments. EMBO J. *41*, e109952. 10.15252/embj.2021109952.

79. Mateju, D., Franzmann, T.M., Patel, A., Kopach, A., Boczek, E.E., Maharana, S., Lee, H.O., Carra, S., Hyman, A.A., and Alberti, S. (2017). An aberrant phase transition of stress granules triggered by misfolded
1620 protein and prevented by chaperone function. EMBO J. *36*, 1669–1687. 10.15252/embj.201695957.

80. Wang, J., Choi, J.-M., Holehouse, A.S., Lee, H.O., Zhang, X., Jahnel, M., Maharana, S., Lemaitre, R., Pozniakovsky, A., Drechsel, D., et al. (2018). A Molecular Grammar Governing the Driving Forces for Phase Separation of Prion-like RNA Binding Proteins. Cell *174*, 688-699.e16. 10.1016/j.cell.2018.06.006.

81. Grese, Z.R., Bastos, A.C., Mamede, L.D., French, R.L., Miller, T.M., and Ayala, Y.M. (2021). Specific RNA interactions promote TDP-43 multivalent phase separation and maintain liquid properties. EMBO Rep. *22*, e53632. 10.15252/embr.202153632.

82. Maury, Y., Côme, J., Piskorowski, R.A., Salah-Mohellibi, N., Chevaleyre, V., Peschanski, M., Martinat, C., and Nedelec, S. (2015). Combinatorial analysis of developmental cues efficiently converts human pluripotent stem cells into multiple neuronal subtypes. Nat. Biotechnol. *33*, 89–96. 10.1038/nbt.3049.

83. Arrigucci, R., Bushkin, Y., Radford, F., Lakehal, K., Vir, P., Pine, R., Martin, D., Sugarman, J., Zhao, Y., Yap, G.S., et al. (2017). FISH-Flow, a protocol for the concurrent detection of mRNA and protein in single cells using fluorescence in situ hybridization and flow cytometry. Nat. Protoc. *12*, 1245–1260. 10.1038/nprot.2017.039.

84. Koehler, L.C., Grese, Z.R., Bastos, A.C.S., Mamede, L.D., Heyduk, T., and Ayala, Y.M. (2022). TDP-43 Oligomerization and Phase Separation Properties Are Necessary for Autoregulation. Front. Neurosci. *16*, 818655. 10.3389/fnins.2022.818655.

85. Lukavsky, P.J., Daujotyte, D., Tollervey, J.R., Ule, J., Stuani, C., Buratti, E., Baralle, F.E., Damberger, F.F., and Allain, F.H.-T. (2013). Molecular basis of UG-rich RNA recognition by the human splicing factor TDP-43. Nat. Struct. Mol. Biol. *20*, 1443–1449. 10.1038/nsmb.2698.

86. Scott, D.D., Francois-Moutal, L., Kumirov, V.K., and Khanna, M. (2019). 1H, 15N and 13C backbone assignment of apo TDP-43 RNA recognition motifs. Biomol. NMR Assign. *13*, 163–167. 10.1007/s12104-018-09870-x.

87. Skinner, S.P., Fogh, R.H., Boucher, W., Ragan, T.J., Mureddu, L.G., and Vuister, G.W. (2016). CcpNmr AnalysisAssign: a flexible platform for

1655 integrated NMR analysis. J. Biomol. NMR *66*, 111–124. 10.1007/s10858-016-0060-y.

88. Best, R.B., Zheng, W., and Mittal, J. (2014). Balanced Protein-Water Interactions Improve Properties of Disordered Proteins and Non-Specific Protein Association. J. Chem. Theory Comput. *10*, 5113–5124. 1660 10.1021/ct500569b.

89. Tang, W.S., Fawzi, N.L., and Mittal, J. (2020). Refining All-Atom Protein Force Fields for Polar-Rich, Prion-like, Low-Complexity Intrinsically Disordered Proteins. J. Phys. Chem. B *124*, 9505–9512. 10.1021/acs.jpcb.0c07545.

1665 90. Abascal, J.L.F., and Vega, C. (2005). A general purpose model for the condensed phases of water: TIP4P/2005. J. Chem. Phys. *123*, 234505. 10.1063/1.2121687.

91. Luo, Y., and Roux, B. (2010). Simulation of Osmotic Pressure in Concentrated Aqueous Salt Solutions. J. Phys. Chem. Lett. *1*, 183–189. 1670 10.1021/jz900079w.

92. Kuo, P.-H., Chiang, C.-H., Wang, Y.-T., Doudeva, L.G., and Yuan, H.S. (2014). The crystal structure of TDP-43 RRM1-DNA complex reveals the specific recognition for UG- and TG-rich nucleic acids. Nucleic Acids Res. *42*, 4712–4722. 10.1093/nar/gkt1407.

1675 93. Afroz, T., Hock, E.-M., Ernst, P., Foglieni, C., Jambeau, M., Gilhespy, L.A.B., Laferriere, F., Maniecka, Z., Plückthun, A., Mittl, P., et al. (2017). Functional and dynamic polymerization of the ALS-linked protein TDP-43 antagonizes its pathologic aggregation. Nat. Commun. *8*, 45. 10.1038/s41467-017-00062-0.

1680 94. Roy, U., and Luck, L.A. (2007). Molecular modeling of estrogen receptor using molecular operating environment. Biochem. Mol. Biol. Educ. *35*, 238–243. 10.1002/bmb.65.

95. Zheng, W., Dignon, G.L., Jovic, N., Xu, X., Regy, R.M., Fawzi, N.L., Kim, Y.C., Best, R.B., and Mittal, J. (2020). Molecular Details of Protein 1685 Condensates Probed by Microsecond Long Atomistic Simulations. J. Phys. Chem. B *124*, 11671–11679. 10.1021/acs.jpcb.0c10489.

96. Regy, R.M., Thompson, J., Kim, Y.C., and Mittal, J. (2021). Improved coarse-grained model for studying sequence dependent phase separation of disordered proteins. Protein Sci. *30*, 1371–1379. 10.1002/pro.4094.

97. Vitalis, A., and Pappu, R. V (2009). Methods for Monte Carlo simulations of biomacromolecules. Annu. Rep. Comput. Chem. *5*, 49–76. 10.1016/S1574-1400(09)00503-9.

98. Páll, S., Zhmurov, A., Bauer, P., Abraham, M., Lundborg, M., Gray, A., Hess, B., and Lindahl, E. (2020). Heterogeneous parallelization and acceleration of molecular dynamics simulations in GROMACS. J. Chem. Phys. *153*, 134110. 10.1063/5.0018516.

99. Evans, D.J., and Holian, B.L. (1985). The Nose–Hoover thermostat. J. Chem. Phys. *83*, 4069–4074. 10.1063/1.449071.

100. Berendsen, H.J.C., Postma, J.P.M., van Gunsteren, W.F., DiNola, A., and Haak, J.R. (1984). Molecular dynamics with coupling to an external bath. J. Chem. Phys. *81*, 3684–3690. 10.1063/1.448118.

101. Y. Zhang, Ö. D. Akyildiz, T. Damoulas, and S. Sabanis (2019). Nonasymptotic estimates for Stochastic Gradient Langevin Dynamics under local conditions in nonconvex optimization. arXiv.

102. Eastman, P., Swails, J., Chodera, J.D., McGibbon, R.T., Zhao, Y., Beauchamp, K.A., Wang, L.-P., Simmonett, A.C., Harrigan, M.P., Stern, C.D., et al. (2017). OpenMM 7: Rapid development of high performance algorithms for molecular dynamics. PLoS Comput. Biol. *13*, e1005659. 10.1371/journal.pcbi.1005659.

103. Darden, T., York, D., and Pedersen, L. (1993). Particle mesh Ewald: An $N \cdot \log(N)$ method for Ewald sums in large systems. J. Chem. Phys. *98*, 10089–10092. 10.1063/1.464397.

104. Ryckaert, J.-P., Ciccotti, G., and Berendsen, H.J.. (1977). Numerical integration of the cartesian equations of motion of a system with constraints: molecular dynamics of n-alkanes. J. Comput. Phys. *23*, 327–341. 10.1016/0021-9991(77)90098-5.

105. Kabsch, W., and Sander, C. (1983). Dictionary of protein secondary

structure: pattern recognition of hydrogen-bonded and geometrical features. Biopolymers *22*, 2577–2637. 10.1002/bip.360221211.

106. Anderson, J.A., Glaser, J., and Glotzer, S.C. (2020). HOOMD-blue: A Python package for high-performance molecular dynamics and hard particle Monte Carlo simulations. Comput. Mater. Sci. *173*, 109363. 10.1016/j.commatsci.2019.109363.

107. Kelley, F.M., Favetta, B., Regy, R.M., Mittal, J., and Schuster, B.S. (2021). Amphiphilic proteins coassemble into multiphasic condensates and act as biomolecular surfactants. Proc. Natl. Acad. Sci. U. S. A. *118*. 10.1073/pnas.2109967118.

Figure 1. TDP-43 undergoes intra-condensate demixing inside stress granules and results in pathological aggregates

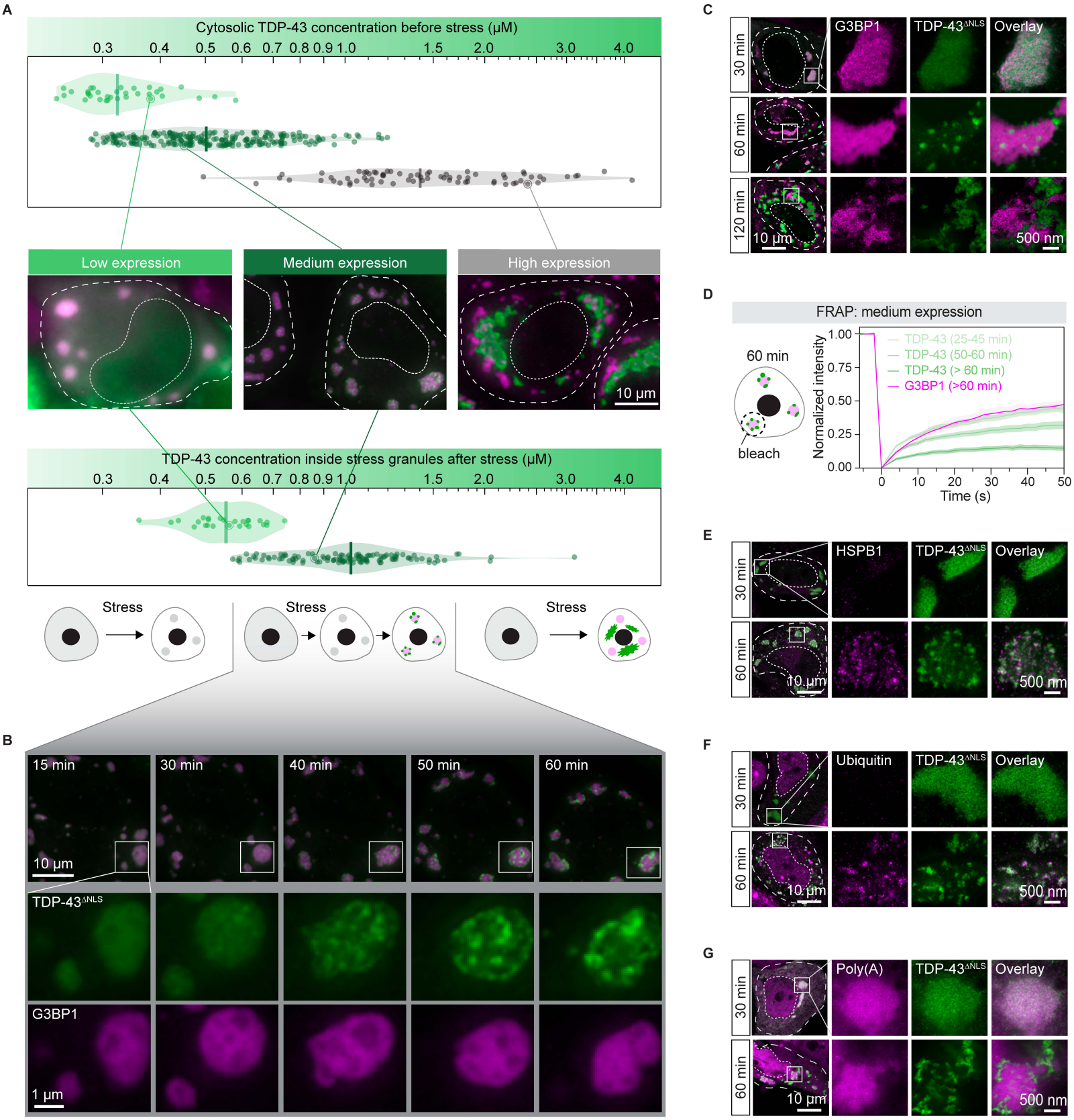

Figure 2. Intra-condensate demixing of TDP-43 promotes a liquid-to-solid phase transition in reconstituted stress granules

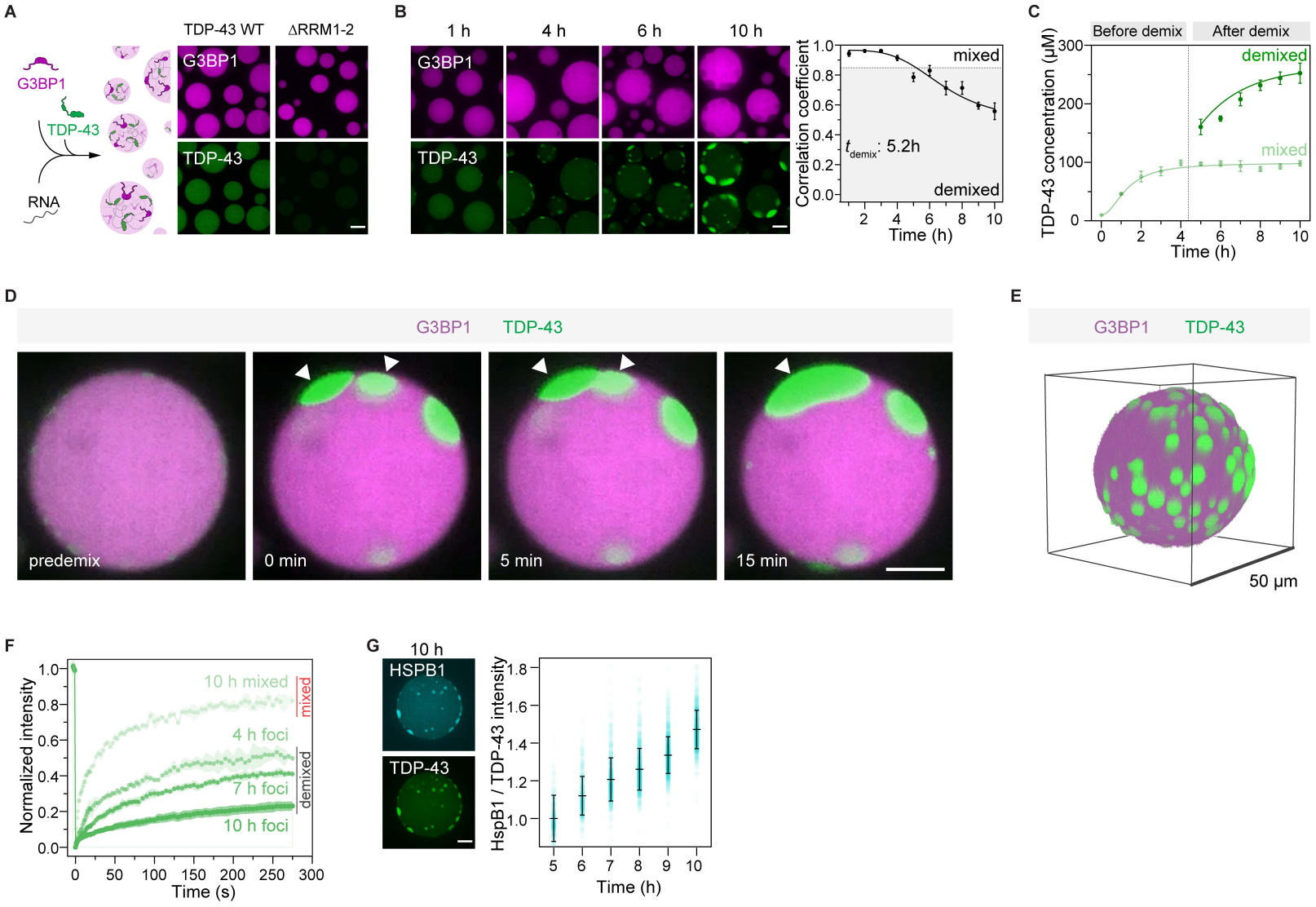

Figure 3. Oxidation is a prerequisite for intra-condensate demixing of TDP-43

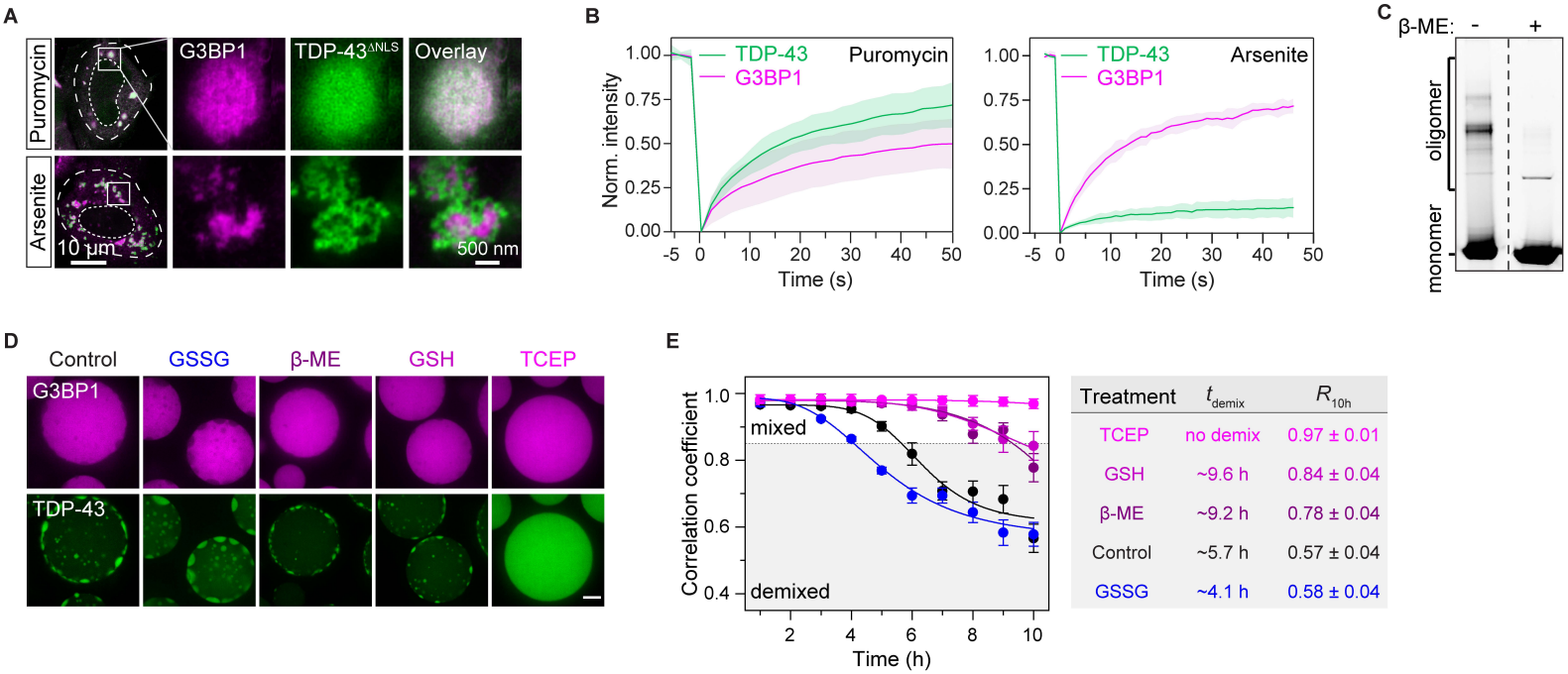

Treatment	t_{demix}	R_{10h}
TCEP	no demix	0.97 ± 0.01
GSH	~9.6 h	0.84 ± 0.04
β-ME	~9.2 h	0.78 ± 0.04
Control	~5.7 h	0.57 ± 0.04
GSSG	~4.1 h	0.58 ± 0.04

Figure 4. Hydrophobic patch interactions and disulfide bond formation constitute homotypic TDP-43 interactions that govern intra-condensate demixing

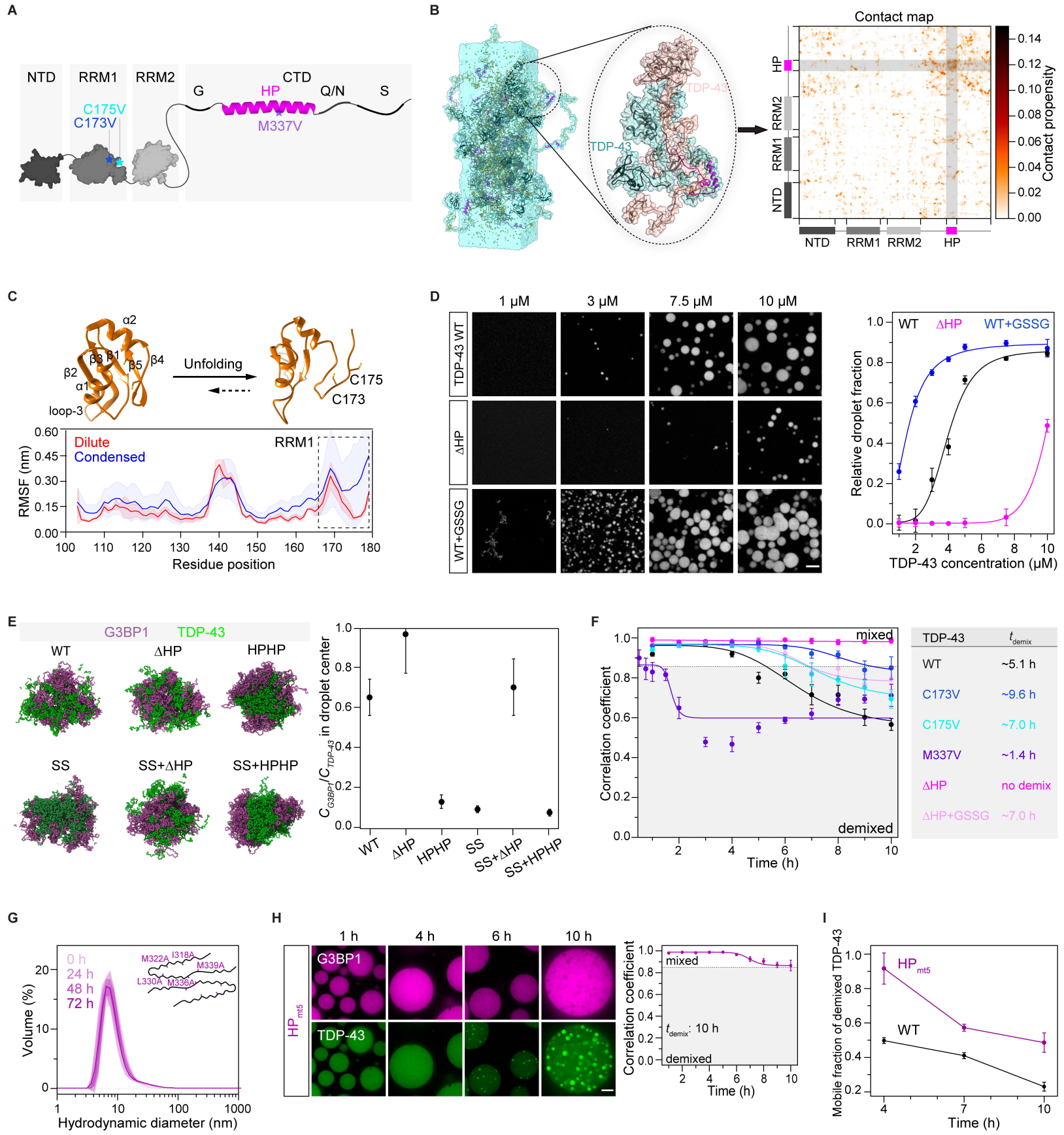

Figure 5. Oxidation-resistant TDP-43 variants with lowered self-assembly propensity abrogate pathological demixing *in vivo*

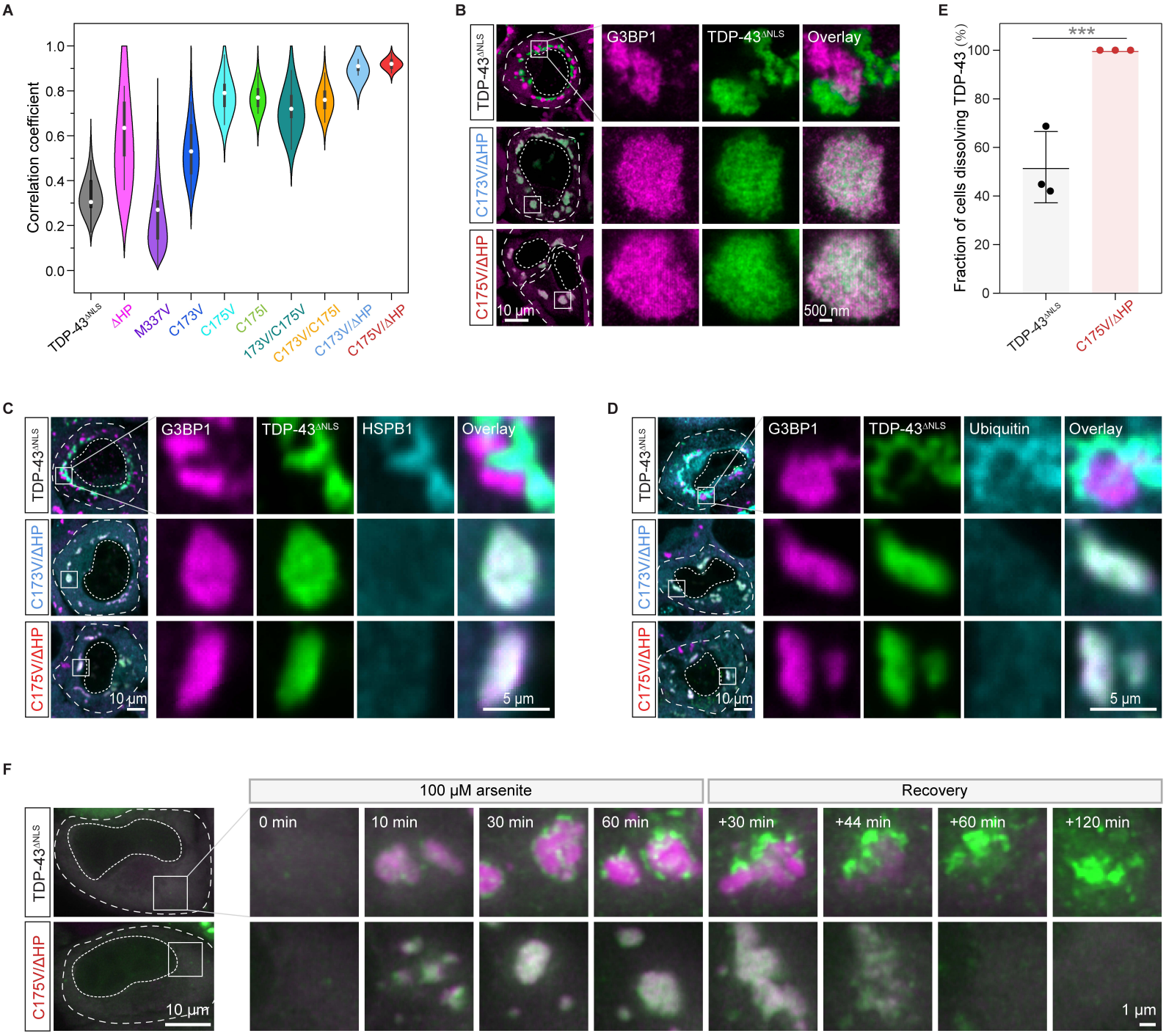

Figure 6. Intra-condensate demixing results in pathological aggregates in motor neurons, accompanied by impairment of nucleocytoplasmic transport

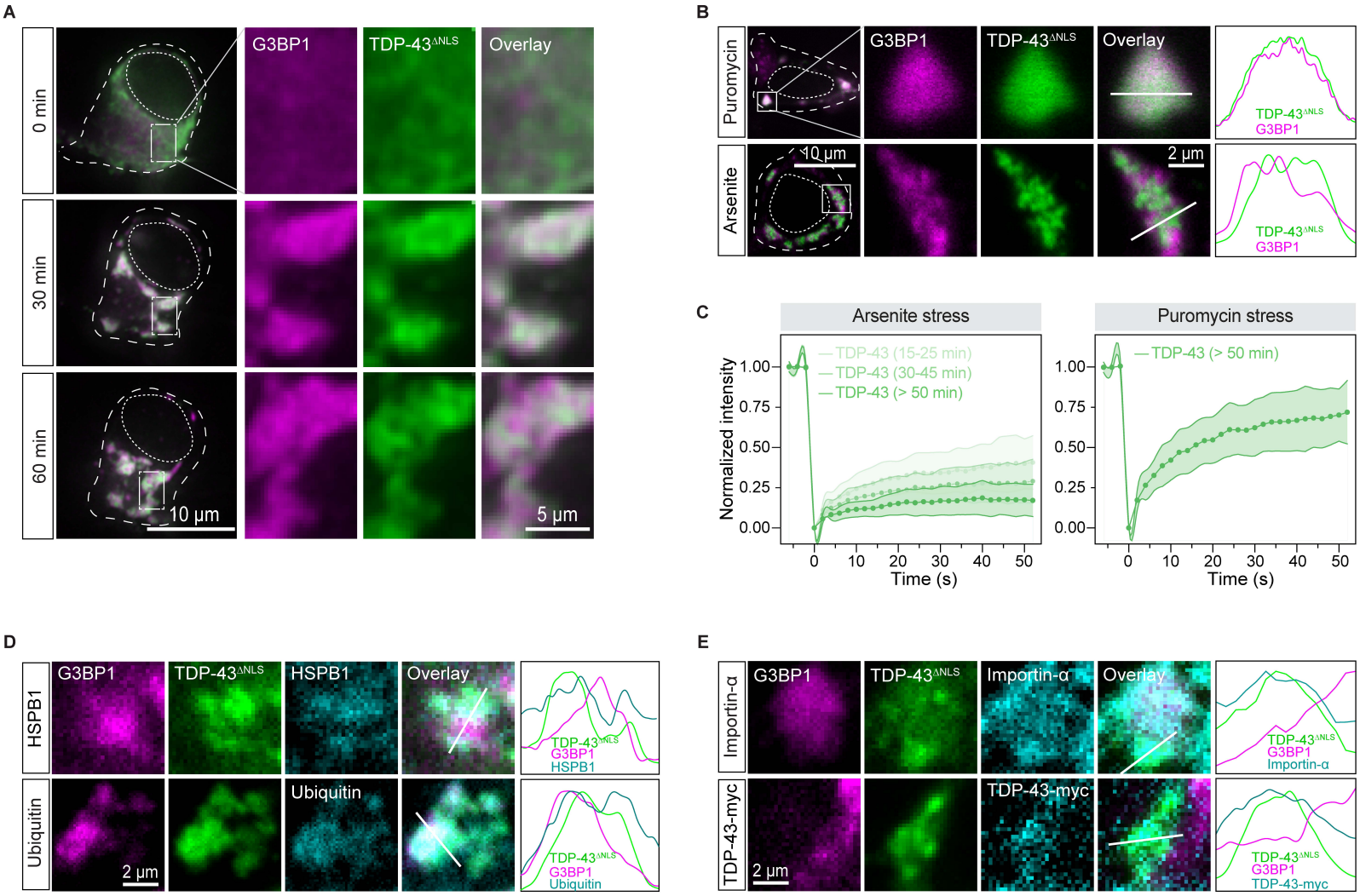

Figure 7. Model of intra-condensate demixing of TDP-43 inside stress granules generating pathological aggregates

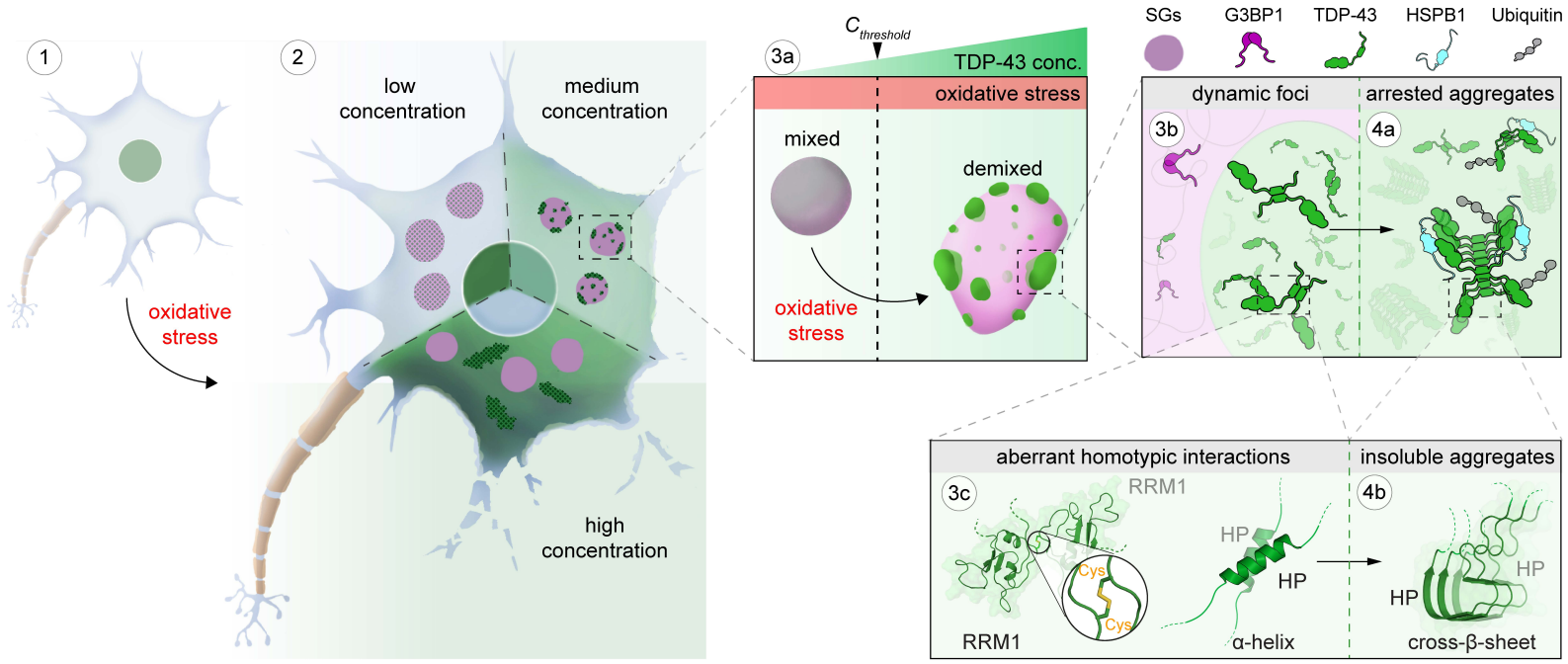

Figure S1. Intra-condensate demixing and aggregate formation of TDP-43 *in vivo*, related to Figure 1

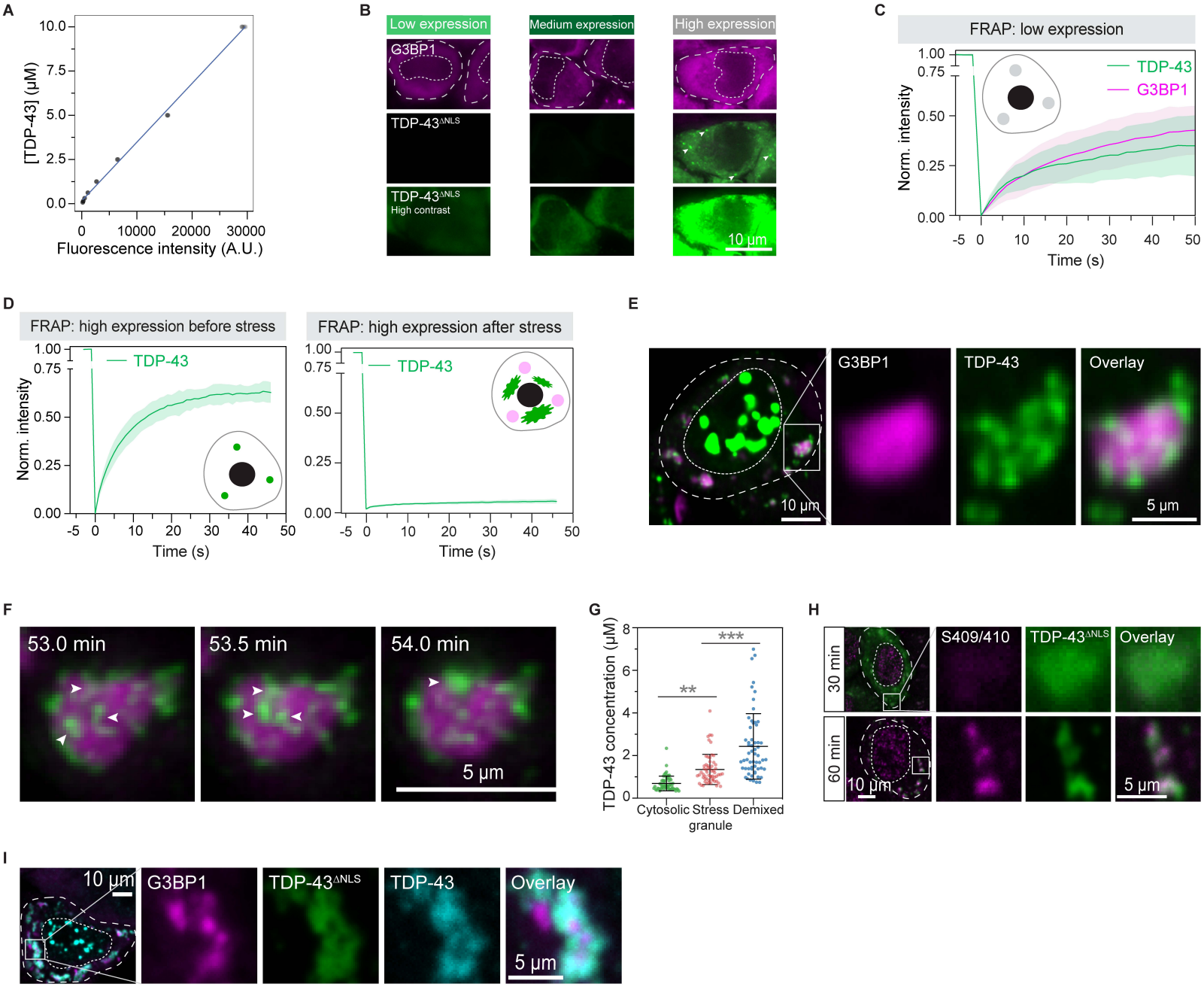

Figure S2. Intra-condensate demixing and aggregate formation of TDP-43 in reconstituted stress granules, related to Figure 2

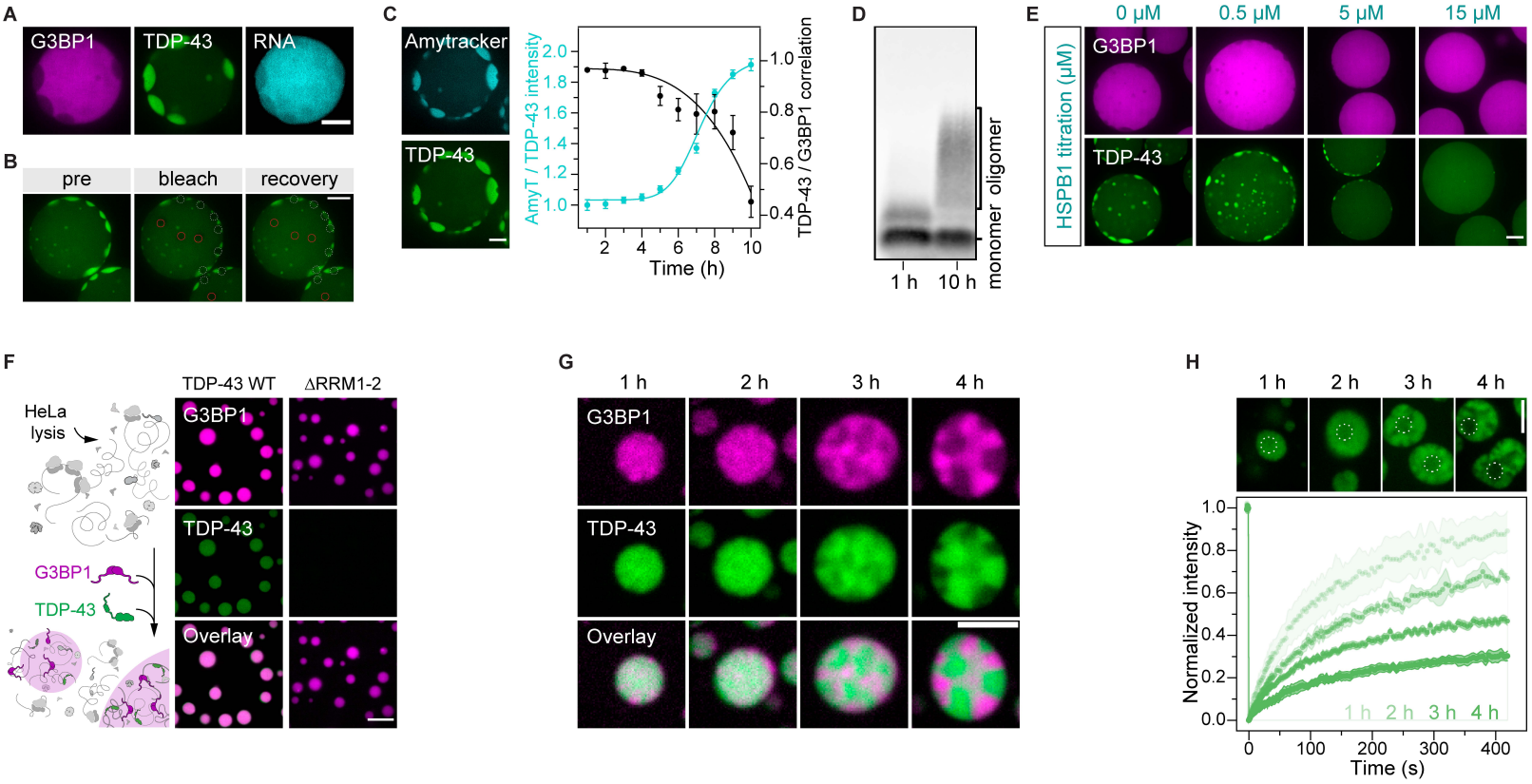

Figure S3. Oxidation is required for intra-condensate demixing of TDP-43, related to Figure 3

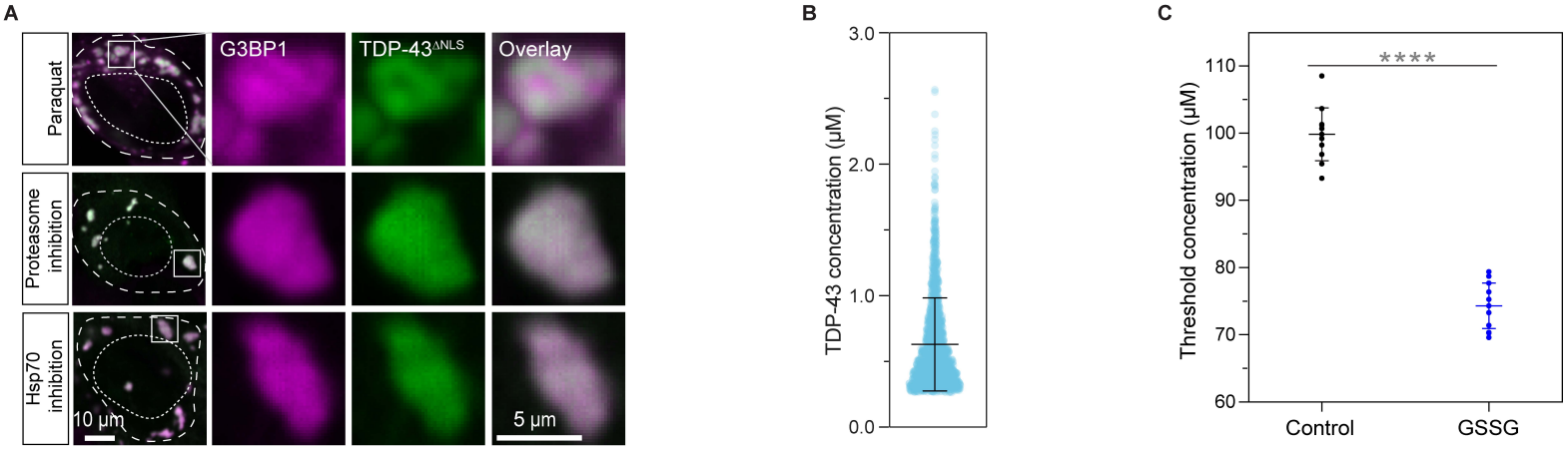

Figure S4. Homotypic interactions mediated by HP interactions and disulfide bond formation govern TDP-43 demixing, related to Figure 4

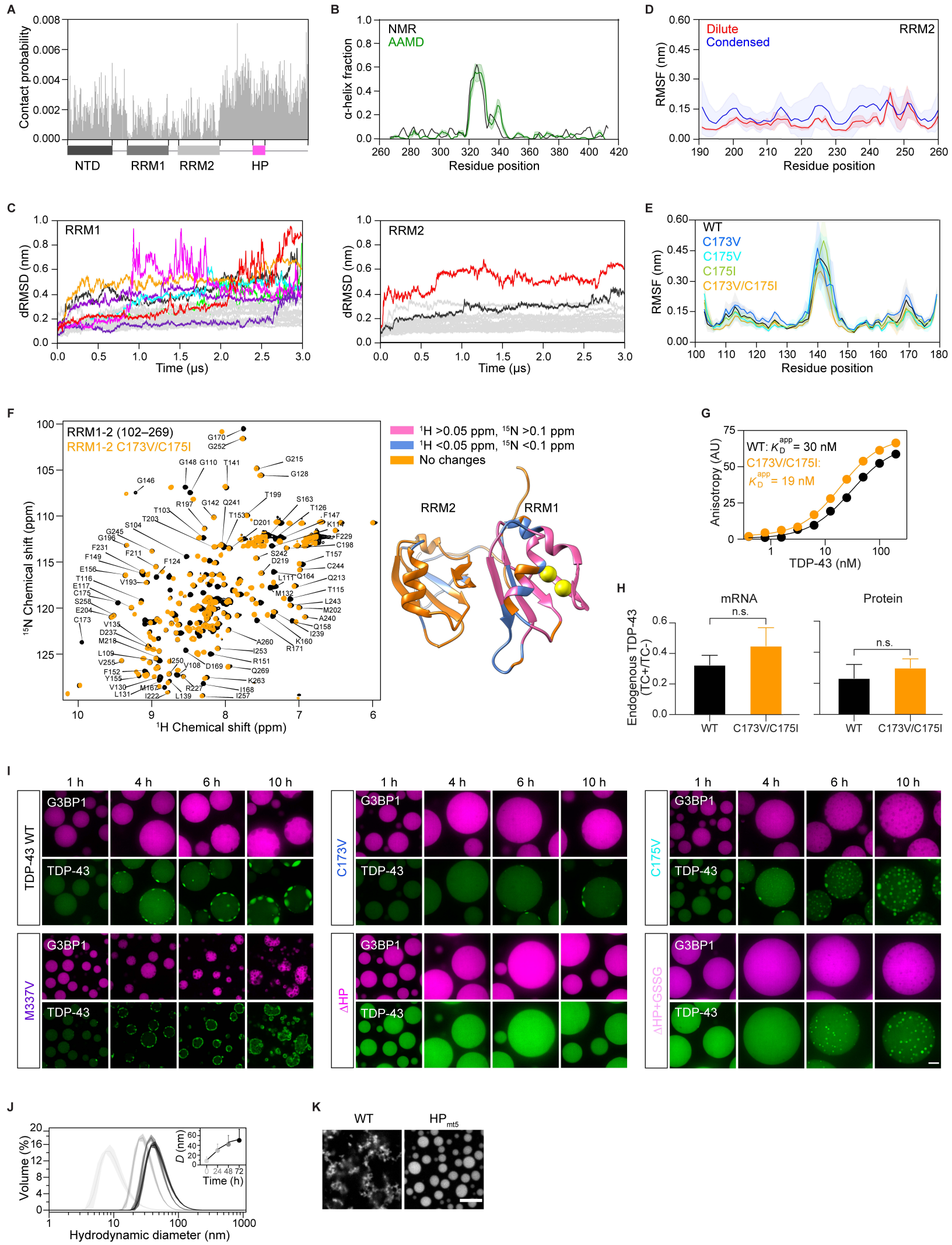
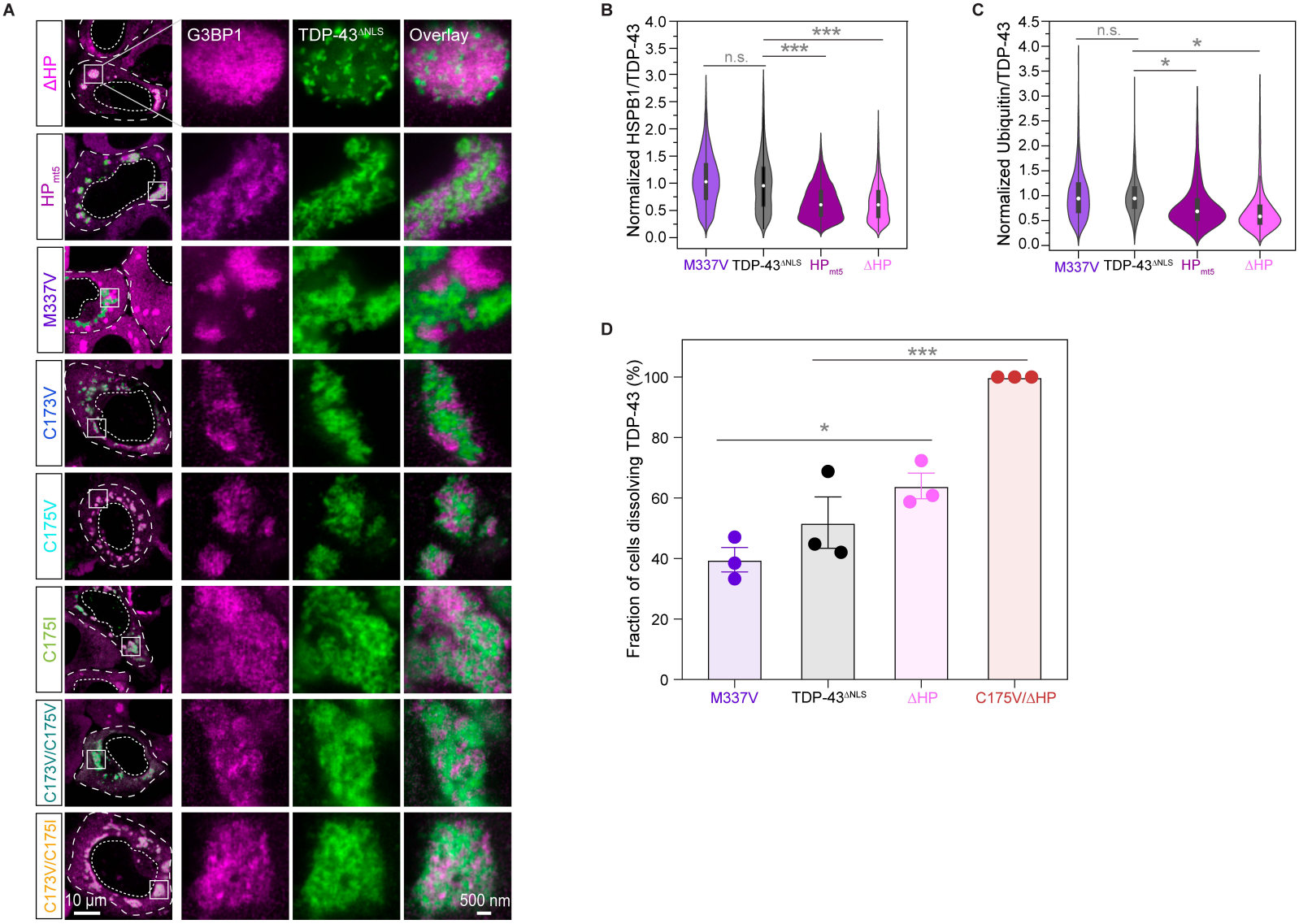
Figure S5. TDP-43 variants with oxidation-resistance and lowered self-assembly propensity abrogate demixing and aggregation *in vivo*, related to Figure 5